On the evolutionary stage of the unclassified B[e] star CD-42°11721†

M. Borges Fernandes,[1]★ M. Kraus,[2]★ S. Lorenz Martins[1]★ and F. X. de Araújo[3]★

[1]*Observatório do Valongo - UFRJ, Ladeira do Pedro Antônio 43, 20080-090, Saúde, Rio de Janeiro, Brazil*
[2]*Astronomický ústav, Akademie věd České republiky, Fričova 298, 251 65 Ondřejov, Czech Republic*
[3]*Observatório Nacional-MCT, Rua General José Cristino 77, 20921-400, São Cristóvão, Rio de Janeiro, Brazil*

ABSTRACT

The star CD-42°11721 is a curious B[e] star sometimes pointed as an evolved B[e] supergiant and sometimes as a young HAeBe star, due to very uncertain or even unknown stellar parameters, especially the distance. In this paper, we present new data gained from high-resolution optical spectroscopy and a detailed description of infrared (IR) data of this star. We present a qualitative study of the numerous emission lines in our optical spectra and the classification of their line profiles, which indicate a non-spherically symmetric circumstellar environment. The first real detection of numerous [Fe II] emission lines and of many other permitted and forbidden emission lines is reported. From our optical data, we derive an effective temperature of $T_{\mathrm{eff}} = 14\,000 \pm 1000$ K, a radius of $R_* = 17.3 \pm 0.6\,\mathrm{R}_\odot$, as well as a luminosity of $L_* = (1.0 \pm 0.3) \times 10^4\,\mathrm{L}_\odot$. We advocate that CD-42°11721 might be a post-main-sequence object, even though a pre-main-sequence nature cannot be ruled out due to the uncertain distance. We further found that the spectral energy distribution in the optical and IR can best be fitted with an outflowing disc-forming wind scenario rather than with a spherical symmetric envelope or with a flared disc, supporting our tentative classification as a B[e] supergiant.

Key words: line: identification – stars: emission-line, Be – stars: individual: CD-42°11721.

1 INTRODUCTION

CD-42°11721 (V921 Sco, Hen 3−1300, IRAS 16555−4237) is a very interesting galactic southern object showing the B[e] phenomenon. B[e] stars are stars of spectral type B with an optical spectrum showing strong Balmer line emission in combination with a large amount of permitted Fe II lines and forbidden O I and Fe II lines. In addition, these stars exhibit a strong near- and mid-infrared (mid-IR) excess due to circumstellar dust.

This star was observed by Merrill & Burwell (1949), who noted a peculiar nature in its spectrum. Due to the presence of a nebulosity around it (Glass & Allen 1975) and possible spectral and photometric variations (Herbst 1975; Carlson & Henize 1979), it was tentatively classified as an HAeBe star (de Winter & Thé 1990; Thé, de Winter & Perez 1994). Based on a possible high temperature and luminosity, Voors (1999) has suggested that CD-42°11721 might be a young star but not a pre-main-sequence object, while spectral similarities among CD-42°11721 and CPD-52°9243 (a supergiant candidate, Carlson & Henize 1979) and HD87643 (an unclassified B[e] star, Hutsemékers & Van Drom 1990) increased the confu-

sion about the evolutionary state of this star. An evolved nature was reinforced by Hutsemékers & Van Drom (1990), who claimed the existence of a nebular overabundance of N/O. Other indications for a post-main-sequence evolutionary phase came from the proposed high luminosity of this object by McGregor, Hyland & Hillier (1988) and Shore et al. (1990). This zoo of proposed evolutionary phases for CD-42°11721 has led to the inclusion of this star into the list of unclassified B[e] stars by Lamers et al. (1998). Recently, Habart et al. (2003) and Hamaguchi, Yamauchi & Koyama (2005) suggested that CD-42°11721 might be a member of a cluster of several low- and intermediate-mass sources.

The confusion concerning the evolutionary stage of CD-42°11721 is strictly linked to the absence of reliable physical parameters. Since the optical spectrum does not display any photospheric lines, the spectral type derived using different sets of observations and methods, varies between B0 and Aep and, consequently, T_{eff} ranges from 31 600 to 12 300 K (Hillenbrand et al. 1992; Cidale, Zorec & Tringaniello 2001). The range in distance is even worse: we found values from 136 pc up to 2.6 kpc (Shore et al. 1990; de Winter & Thé 1990; Elia et al. 2004). Consequently, its luminosity is not known either, being in the range $1.9 < \log(L/\mathrm{L}_\odot) < 4.9$ (McGregor et al. 1988; Shore et al. 1990; Hillenbrand et al. 1992). These uncertain stellar parameters and therefore the rather poor knowledge of the evolutionary phase of CD-42°11721 have stimulated us to investigate this object in more detail, based on a multiwavelength analysis.

★E-mail: borges@ov.ufrj.br (MBF); kraus@sunstel.asu.cas.cz (MK); slorenz@ov.ufrj.br (SLM); araujo@on.br (FXdeA)
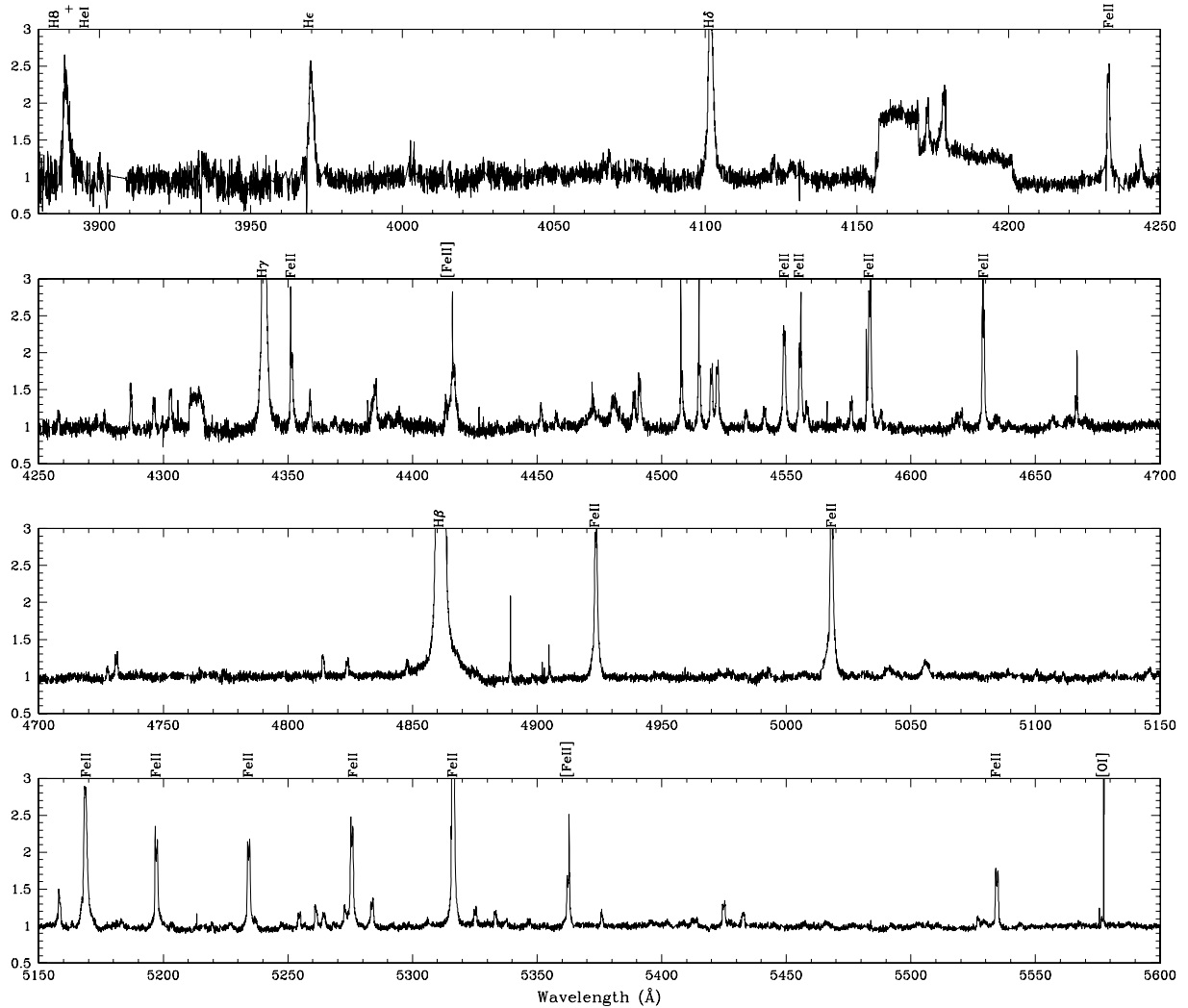
Figure 1. The FEROS spectrum of CD-42°11721. The most intense emission lines are indicated. A list of all identified lines is given in Table A1 in Appendix A.

In this paper, we are presenting new high- and low-resolution optical spectra together with a more detailed description of available IR data taken from both the public catalogues and the literature. We obtained a detailed optical spectral atlas, where the zoo of emission lines (many of them previously undetected) and the variety in line profiles give hints for the gas dynamics and distribution in the close-by circumstellar medium (CSM) around CD-42°11721. We could also derive a set of stellar parameters based on our high-resolution data, allowing to compare the position of CD-42°11721 in the Hertzsprung–Russell (HR) diagram with evolutionary tracks. Considering these stellar parameters, we have also modelled its spectral energy distribution (SED) considering different circumstellar scenarios: a spherically symmetric geometry, a passive flared disc and also an outflowing disc wind.

The structure of this paper is as follows. In Section 2, we describe our observations, the data reduction and the public data used. Section 3 gives a detailed optical spectral atlas and a description of the zoo of emission lines and the variety in line profiles found. In Section 4, we present a description of the IR region. On the basis of our optical spectra we derive in Section 5 the stellar parameters. In Section 6, we describe the SED modelling of this star, presenting the numerical codes developed by us, the results obtained and

also the comparison between them and the literature ones. In Section 7, we discuss the possible nature of CD-42°11721 and present the conclusions of our study.

2 OBSERVATIONS AND REDUCTIONS

Our optical spectra were obtained at the European Southern Observatory (ESO) 1.52-m telescope in La Silla (Chile) using the high-resolution Fiber-fed Extended Range Optical Spectrograph (FEROS) and the low-resolution Boller & Chivens spectrograph.

FEROS is a bench-mounted Echelle spectrograph with fibres, that cover a sky area of 2 arcsec in diameter, with a wavelength coverage from 3600 to 9200 Å and a mean spectral resolution of $R = 48\,000$ corresponding to 2.2 pixel of 15 μm. It has a complete automatic online reduction, which we adopted. Our FEROS spectrum presents the highest resolution used for observations of CD-42°11721 to date. It was taken on 2000 June 10, with an exposure time of 5400 s. The signal-to-noise ratio (S/N) in the 5500-Å region is approximately 60. This high-resolution spectrum and long wavelength coverage, shown in Fig. 1 will be used to obtain a detailed optical spectral atlas, for a detailed description of the different line profiles, to derive
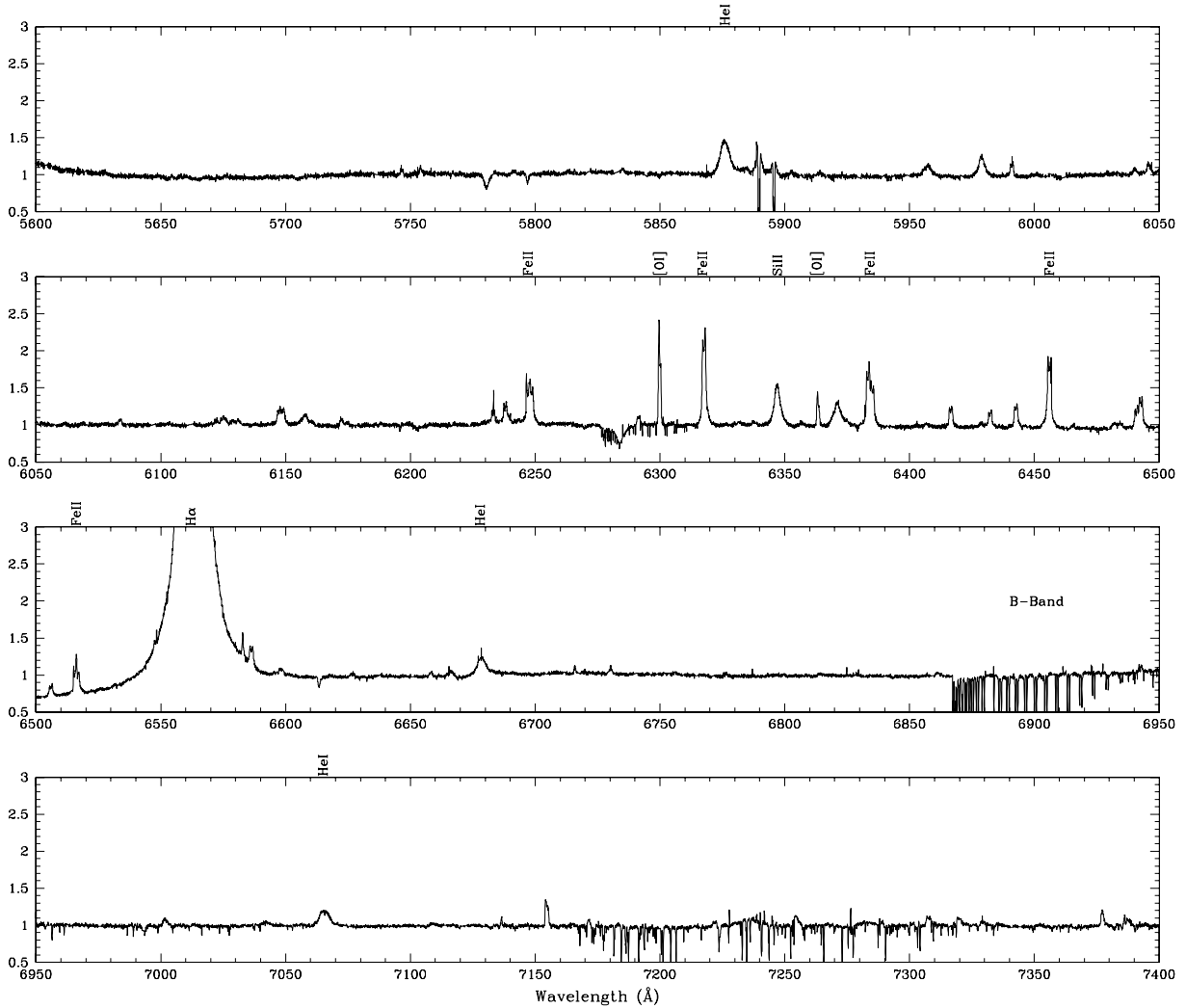
Figure 1 – *continued*

equivalent widths, and also to deblend some features in the low-resolution spectra.

The low-resolution Boller & Chivens spectrum (hereafter Cassegrain spectrum) was taken on the same observation run at ESO, but on 2000 June 9, with an exposure time of 900 s. The instrumental set-up employed made use of grating #23 with 600 l mm^{-1}, providing a resolution of $\sim$4.6 Å in the range 3800–8700 Å. In the 5500-Å continuum region, the S/N of the Cassegrain spectrum is approximately 180. Since there is no completely line-free region in the spectrum, the S/N derived is an upper limit. The slit width used was 2 arcsec. Considering that the nebula in which CD-42°11721 is embedded has dimensions of $\sim$40 × 80 arcsec^2 (Hutsemékers & Van Drom 1990), our observations were centred on the innermost parts of it. The Cassegrain spectrum was reduced using standard IRAF tasks, such as bias subtraction, flat-field normalization, and wavelength calibration. We have done absolute flux calibration using spectrophotometric standards from Hamuy et al. (1994). This spectrum is used to derive intensities of the emission lines for which we perform a detailed quantitative analysis.

Equivalent widths and line intensities in the linearized spectra have been measured using the IRAF task that computes the line area above the adopted continuum. Uncertainties in our measurements come mainly from the position of the underlying continuum and

we estimate the errors to be about 20 per cent for the weakest lines (equivalent widths lower than 2 Å) and about 10 per cent for the strongest lines.

We have also obtained photometric data from the literature, intending to describe the complete SED of CD-42°11721. In addition, we have described the IR spectra obtained by *ISO* and *IRAS* satellites. These spectra are public and can be downloaded from the following web addresses: SWS01-*ISO*–http://isc.astro.cornell.edu/~sloan/library/swsatlas/aot1.html; LRS-*IRAS* – http://www.iras.ucalgary.ca/~volk/getlrs_plot.html. The *IRAS* LRS spectrum covers a small wavelength range, from 7.5 to 22 μm, with a spectral resolution of about 20–60. On the other hand, the *ISO* SWS01 spectrum has a higher resolution of $\sim$1500 and a wavelength coverage from 2 to 50 μm.

3 THE OPTICAL SPECTRAL ATLAS: EMISSION LINES AND THEIR PROFILES

To identify the lines and to create a spectral atlas of the optical region of CD-42°11721, we have used the line lists provided by Moore (1945), Thackeray (1967), Hamann & Persson (1989), McKenna et al. (1997) and Landaberry, Pereira & de Araújo (2001). We have also looked up two sites on the web: NIST Atomic Spectra
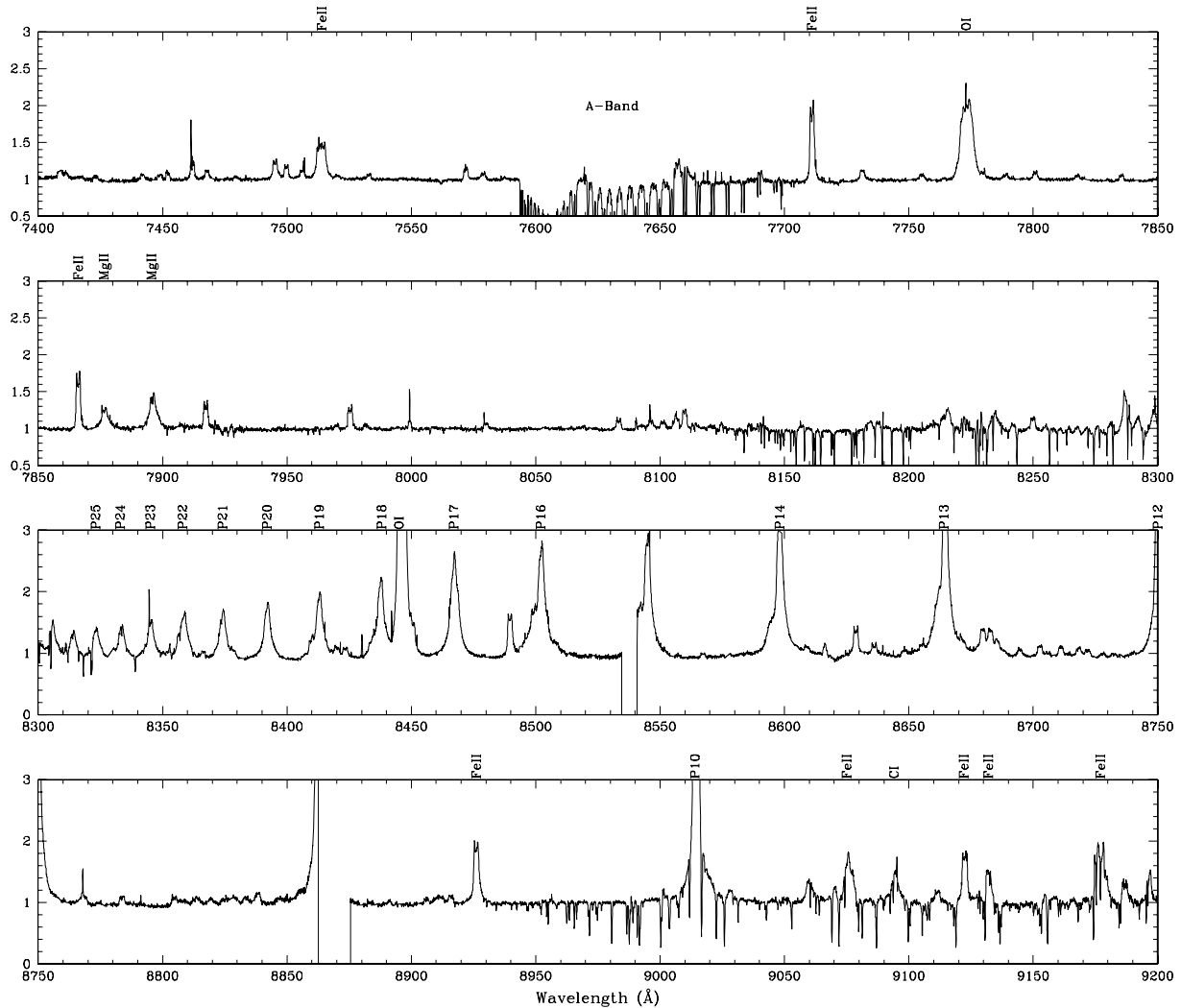
Figure 1. – *continued*

Fig. 1 shows the complete high-resolution spectrum of CD-42°11721. It is completely dominated by emission lines. The only absorption lines visible are the Ca II and Na I lines, which are of interstellar origin, as well as the diffuse interstellar bands (DIBs). Our spectra do not exhibit any photospheric lines.

A huge number of permitted and forbidden emission lines were identified in the FEROS spectrum of CD-42°11721 and listed in Table A1 given in Appendix A. The individual columns in Table A1 contain the observed wavelength (Column 1), equivalent width [W(λ) in Å, Column 2], the line profile type (Column 3), and the proposed identification (Column 4) for each line. The line identification given in Column 4 encloses the ionization state of the element with the proposed transition and multiplet as well as the rest wavelength of the transition. It is possible that more than one ion can be allocated to a single feature. In these cases, we give some possible alternative identifications. For some lines no identification could be found. These lines remain unidentified, labelled as 'Uid' in the tables.

An inspection of Table A1 reveals a huge zoo of emission lines from atoms mostly singly ionized, as well as a variety in their line profiles. Interestingly, there are also many emission lines from neutral metals like C I, N I and O I, and some sporadic traces for the emission of S I and Mg I as well. Many of the lines listed in Table A1 are detected by the first time.

In the following, we briefly discuss the presence of individual elements and lines and, if possible, compare our observations with previously published data. We especially highlight deviations of our observations from data in the literature which all seem to point in favour of either central source variability or ongoing changes in the CSM conditions. In addition, we classify the different line profiles.

3.1 The zoo of emission lines

(i) *Hydrogen.* The strongest lines in the spectra of CD-42°11721 are the Balmer lines (Fig. 2). We could identify the Balmer series up to H9 at the blue edge of our spectrum. While Hα, Hβ and Hγ show indications for a double-peaked profile and broad wings extending to velocities of about 1400, 600 and 200 km s^{-1} respectively (for the Hα wings see Fig. 3), the higher Balmer lines are singly peaked and their wing velocities decrease systematically. The equivalent width of Hα is almost a factor of 2.5 lower than the value reported by Lopes, Damineli Neto & de Freitas Pacheco (1992). The Hβ equivalent width has also been reported to be variable
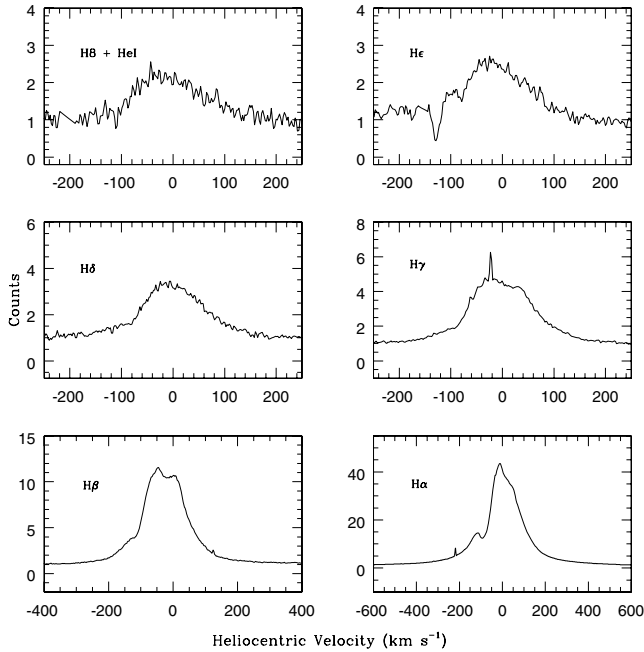
Figure 2. Balmer lines from the CD-42°11721 high-resolution (FEROS) spectrum. The lines are broad and in emission with Hα, Hβ and Hγ showing indications for a double-peaked profile. The absorption dip within the blue wing of Hε is the interstellar Ca II 3968 Å line. Due to the scale of these figures, the extended wings of especially the Hα and Hβ lines cannot be seen.
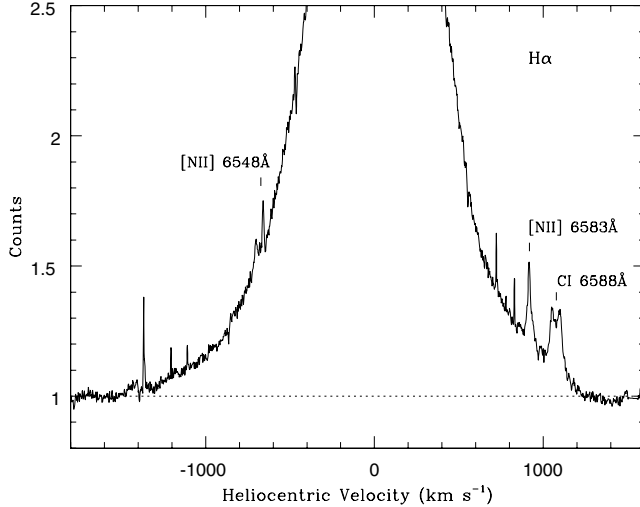

Figure 3. The wings of the Hα line, extending to ~1400 km s^{-1}. The C I λ 6588 as well as the [N II] λλ 6548, 6583 lines are also indicated. The dotted line represents the continuum.

(Lopes et al. 1992). While it was found to be 27.7 Å in the 1985 observations, it increased to 41.5 Å in the 1988 observations. Our value, observed in 2000, lies with 30.4 Å in between.

In addition, at the long-wavelength end of the spectrum, the Paschen series arises. From this series we could clearly identify the lines from Pa(10) up to Pa(40). Their profiles are all narrow and single-peaked (see Fig. 1).

(ii) *Helium.* Helium seems to be variable in the spectrum of CD-42°11721. While it had (possibly) been detected in the years 1945–
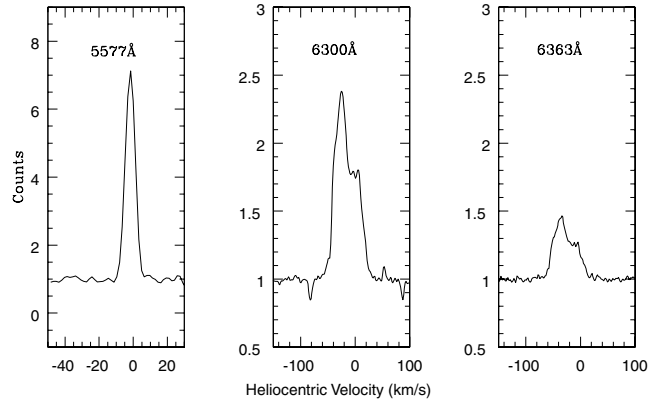

Figure 4. The [O I] lines at 5577, 6300 and 6363 Å. Except the λ 5577 line, these lines are double-peaked with a missing red peak.

1948 by Merrill & Burwell (1949), it was absent in the spectra of Carlson & Henize (1979) taken in 1949–1951 and 1962, and re-appeared again in the spectra observed in 1985 by Lopes et al. (1992) and 1989 by Hutsemékers & Van Drom (1990), and also our data which have been taken in 2000 show emission of He I. We do not detect any line from He II.

(iii) *Oxygen.* The detection of the [O I] 6300 Å was the first reported by Acke, van den Ancker & Dullemond (2005). This line (and other oxygen lines) have not been seen during earlier observations performed by de Winter & Thé (1990) and Hutsemékers & Van Drom (1990).

Our data, which have been taken two years earlier than those of Acke et al. (2005), confirm the presence of this emission line, and we can report on numerous additional identifications of emission lines of neutral oxygen, both forbidden and permitted. Interestingly, the [O I] 6300 Å and 6364 Å lines show an asymmetric profile resembling a double-peaked line with a missing red peak, while the 5577-Å line is clearly single-peaked and very narrow compared to the other two lines (Fig. 4). The profile of the [O I] line λ 6300 shown by Acke et al. (2005) agrees with ours, but there are significant differences in the equivalent width of this line: while Acke et al. (2005) derived a value of 1.77 Å, the equivalent width found from our observations is only 1.20 Å. Since the set-up for both observations was quite similar, this difference in equivalent width might hint towards rapidly changing conditions, for example, in density and temperature structure, within the line-forming region.

In addition, we found (though very weak) the previously not-detected [O II] lines λλ 7319, 7330. No single O III line was identified.

(iv) *Nitrogen.* The only previously detected emission line from nitrogen in the spectrum of CD-42°11721 is the line [N II] λ 5755, cited by de Winter & Thé (1990) and Hutsemékers & Van Drom (1990). The latter, however, ascribed the emission to the nebula and could not identify this line in the stellar spectrum. Our high-resolution spectrum confirms the existence of this emission line. In addition, we detected the lines [N II] λλ 6548, 6584, as well as N II λ 6173. Remarkably, we also identified many permitted emission lines from N I.

(v) *Carbon.* The detection of any carbon line has not been reported yet. Our spectrum clearly shows the presence of several lines of C I (see e.g. Fig. 3), one line of C II and C III each, as well as the possible detection of a [C I] line.

(vi) *Sulphur.* The existence of the [S II] λλ 6716, 6731 lines has formerly been reported by Hutsemékers & Van Drom (1990) as

coming from the nebula. In addition to these lines, our spectrum also contains the line [S II] λ 4068 while the λ 4076 line is missing. From S III we could identify only one line, that is, [S III] λ 9069. The line [S III] λ 6311 does not show up in our spectrum. However, as in the case of N, O and C, we have some indications for the presence of S I emission.

(vii) *Iron.* It is the element with by far the largest number of emison lines. With the exception of four lines allocated to Fe III (two forbidden and two permitted), all lines are from singly ionized iron. CD-42°11721 is known to show a huge number of Fe II lines (e.g. Carlson & Henize 1979; Hutsemékers & Van Drom 1990); however, the existence of an equally large amount of [Fe II] lines as we found in our spectrum, has previously not been reported. Actually de Winter & Thé (1990) reported on a possible detection of an [Fe II] line; however, this identification is rather doubtful due to their low spectral resolution. These lines show either single-peaked, double-peaked, or even multiple-peaked profiles, indicating a high complexity of the CSM. The permitted lines are usually more intense than the forbidden ones and also broader with wings extending to 100–200 km s^{-1}, while the line wings of the forbidden lines indicate velocities of about ∼50–60 km s^{-1}, only.

(viii) *Other elements.* In addition, we identified emission lines from the following metal ions: Cr II, Mg I, Mg II, Mn II, Ti II, Si II and Ne II. Most of them have previously not been detected.

3.2 Classification of the line profiles

To understand the structure of the CSM of CD-42°11721, we sort the observed emission-line profiles into three categories (see Table A1): (i) single-peaked, (ii) double-peaked and (iii) multiple-peaked. In agreement with the descriptions in earlier studies (e.g. Lopes et al. 1992), no single P Cygni profile was detected.

(i) *Single-peaked profiles.* These profiles clearly dominate. They can be found without any exception for every element in every ionization stage, independent whether these are forbidden or permitted lines. To draw any conclusion about the dynamics of the CSM, we measured the line wing velocities of several forbidden (and therefore optically thin) emission lines. The results are listed in Table 1, together with the high wing velocities found from the Balmer lines. Following two striking conclusions can be drawn from this table. (i) The mean wing velocity (which we call the expansion velocity, $v_{\rm exp}$) is of the order of 50–60 km s^{-1} and about constant for all the forbidden lines, and (ii) the line centre velocity of all lines is also about constant and of the order of −20 km s^{-1}.

(ii) *Double-peaked profiles.* There are quite a lot of lines showing a double-peaked profile. The blue and red peaks are thereby of equal strength with only some rare exceptions. One remarkable exception is the [O I] lines at 6300 Å and 6364 Å for which the red peak is missing (Fig. 4). Another exception is the Balmer lines, especially Hα and Hβ (see Fig. 2)

In Table 2, we list some of the well-resolved double-peaked lines from the FEROS spectrum together with their peak separation, which lies between 30 and 50 km s^{-1} (neglecting the Balmer lines).

Interestingly, the double-peaked profiles are present only for neutral metals (like O I, N I, C I, and S I) and ions with low ionization potential, that is, lines from Fe II, Mg II, and Cr II with $\chi < 8\,{\rm eV}$, which is well below the ionization potential of hydrogen. This fact has the following two severe implications.

(1) The emitting material must be neutral in hydrogen, and

Table 1. Velocities of the H Balmer lines and some forbidden lines seen in the FEROS spectrum. Listed are the ions, the laboratory wavelength of the line, the blue and red wing velocities, the mean expansion velocity, and the line centre velocity.

Ion	λ (Å)	$v_{\rm blue}$ (km s^{-1})	$v_{\rm red}$ (km s^{-1})	$\langle v_{\rm exp} \rangle$ (km s^{-1})	v_0 (km s^{-1})
Hα	6562	−1500	+1300	1400	−100
Hβ	4861	−500	+600	550	+50
Hγ	4340	−200	+200	200	0
Hδ	4101	−150	+150	150	0
Hε	3970	−140	+140	140	0
H8	3889	−120	+120	120	0
O I	6300	−80	+40	60	−20
O I	6364	−70	+20	45	−25
S II	4068	−60	+30	45	−15
S II	6716	−50	+30	40	−10
S II	6731	−80	+30	55	−25
N II	5755	−80	+20	50	−30
N II	6584	−60	+10	35	−25
Cr II	8106	−90	+40	65	−25
Cr II	8110	−80	+40	60	−20

Table 2. Peak separation of double-peaked lines for different ions.

Ion	Line (Å)	Peak separation (km s^{-1})		Ion	Line (Å)	Peak separation (km s^{-1})
Hα	6562	130		Fe II	5169	40
Hβ	4861	60		Fe II	5197	50
[O I]	6300	40		Fe II	5234	40
[O I]	6364	40		Fe II	5276	40
[Fe II]	5283	40		Fe II	5316	40
[Fe II]	7155	40		Fe II	5534	40
Fe II	4520	30		Fe II	6318	40
Fe II	4549	40		Fe II	7711	50
Fe II	4923	30		Fe II	7866	50
Fe II	5018	40				

(2) the double-peaked profiles might indicate rotation.

Combination of both seems to suggest the existence of a neutral (in hydrogen) rotating disc or an equatorial outflowing wind (see e.g. Zickgraf 2003). However, we emphasize that the double-peaked profiles are not restricted to permitted lines only, but are also present in several forbidden lines from [O I], [Cr II], and of course [Fe II].

(iii) *Multiple-peaked profiles.* These types of profiles are found especially for permitted emission lines of Fe II where three peaks or more are observed. The existence of such multiple-peaked lines favours a highly complex multi-component emission region.

3.3 Comparison with optical spectra of other B[e] stars

Based on low-resolution optical observations, it has been noted in the literature that the spectrum of CD-42°11721 is quite similar to some other B[e] stars. One of these is HD 87643 (Hutsemékers & Van Drom 1990; Oudmaijer et al. 1998), another object belonging to the group of unclassified B[e] stars since it also shows characteristics that might classify this object either as a HAeB[e] stars or as a B[e] supergiant (Lamers et al. 1998). The low-resolution spectra as shown in Fig. 5 are indeed *similar*; however, there exist also differences that show up already in this plot: in contrast to
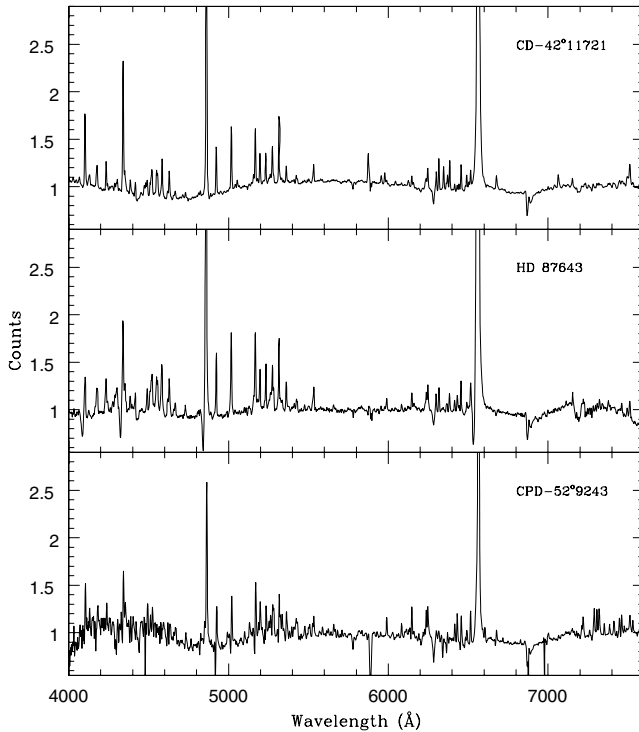
Figure 5. Comparison of the Cassegrain spectra of CD-42°11721 with some other B[e] stars. Though quite similar at the first glance, they show severe differences: the spectrum of HD 87643 does show the presence of P Cygni profiles, and the spectrum of CPD-52°9243 has the He I lines in absorption.

CD-42°11721, the spectrum of HD 87643 clearly shows the presence of P Cygni profiles.

Another object found to exhibit a similar optical low-resolution spectrum (also included in Fig. 5), is CPD-52°9243 (Carlson & Henize 1979; Swings 1981; Winkler & Wolf 1989), a galactic B[e] supergiant candidate (Lamers et al. 1998). The most obvious difference in its optical spectrum is, however, the presence of the He I lines in *absorption*.

For these three stars, high-resolution (FEROS) observations show very clearly that there exist numerous other differences (see Borges Fernandes 2004), which cannot be listed here in detail.

4 THE INFRARED REGION: GAS AND DUST FEATURES

Concerning to the IR region, CD-42°11721 was observed by *ISO* and *IRAS* satellites. The *IRAS* LRS spectrum (Fig. 6) is characterized by a strong absorption centred around 10 μm, originated by amorphous silicate, that is not seen in the *ISO* SWS01 spectra. It was classified by Zhang, Chen & He (2004) as *'noisy or incomplete'*, meaning that the absorption could not be real. Actually, the first part of LRS *IRAS* (from 7.6 to 13.4 μm) is not so noisy and we can clearly see the previously known as 'unidentified IR bands' (UIR) that are commonly accepted nowadays as being caused by vibrational transitions of polycyclic aromatic hydrocarbons (PAHs), at 7.6, 11.3 and 12.7 μm.

The SWS01 *ISO* spectrum (see also Fig. 6) of this object shows especially a strong rising continuum beyond 15 μm, being clearly seen gas and dust emission features (Voors 1999). Concerning the gas emission, remarkable is the presence of many H recombination lines (Benedettini et al. 1998) and also the presence of forbidden
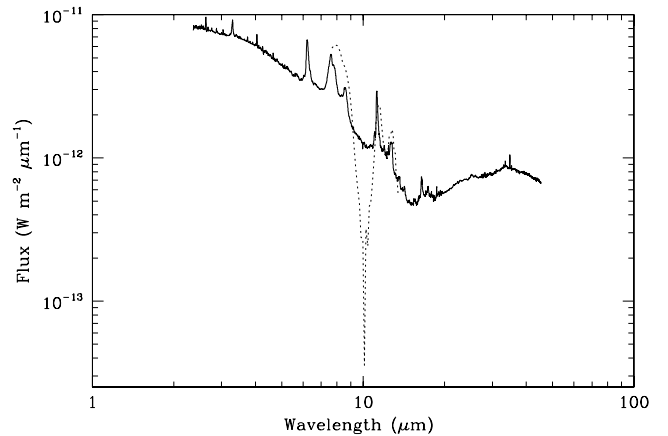

Figure 6. The SWS01 *ISO* spectrum (solid line) and the *IRAS* LRS spectrum (dotted line) of CD-42°11721.

lines, for example, [Si II], [Fe II] and [S III] lines. Other forbidden lines, for example, [O I], [C II], [N II] and [O III] lines, were identified by Lorenzetti et al. (1999) by the analysis of the Long Wavelength Spectrograph (LWS-*ISO*) spectra of this star. We have also tentatively identified some features as being caused by H$_2$ molecule; however, these identifications are very uncertain. McGregor et al. (1988) cited the probable presence of CO bands; however, we could not identify these features in the SWS01 *ISO* spectrum.

Regarding the dust emission, the *ISO*-SWS spectrum presents the called 'dual-dust' chemistry, characterized by the existence of solid state bands of C-rich and O-rich dust in the same environment. The C-rich material is represented by PAH emission bands (Jourdain de Muizon, d'Hendecourt & Geballe 1990; Voors 1999). On the other hand, beyond 20 μm, the O-rich dust is represented by some features caused by crystalline silicates.

In Table 3, we compile the identifications available from different papers and those determined by this work, giving a complete view of the most important features present in the *ISO*-SWS spectrum of CD-42°11721, from 2 to 50 μm. There, the observed wavelength (Column 1), the proposed identification (Column 2), and the reference (Column 3) for each feature are given.

However, all the spectral description cited above, in this section, probably is not related to the star itself. This happens because *ISO* and *IRAS* data cover a large area of the sky around CD-42°11721 and therefore they are probably contaminated by the known surrounding reflection nebula and/or other stars, since it lies in a crowded region (Habart et al. 2003; Hamaguchi et al. 2005). This contamination is clearly shown by Acke & van den Ancker (2006) that presented new IR spectra of the 3- and 10-μm wavelength regions. These spectra cover an area of only 1 arcsec in diameter around CD-42°11721, therefore, the region close-by this star, and surprisingly, they do not present the strong PAH emission seen in the *ISO* and *IRAS* spectra. This fact means that 'dual-dust' chemistry is not related to the object itself.

5 THE STELLAR PARAMETERS OF CD-42°11721

Most of the problems in classifying CD-42°11721 are caused by the uncertain stellar parameters. We therefore use first our optical high-resolution data for a tentative determination of the stellar parameters. The details on how we estimate each parameter are given in this section.

Table 3. The identification of the features present in the *ISO*-SWS spectrum.

λ (μm)	Ident.	Ref.		λ (μm)	Ident.	Ref.
2.39	Pf (23-5)			5.40	Uid	
2.41	Pf (22-5)			5.60	Uid	
2.42	Pf (21-5)			5.70	PAH	V
2.43	Pf (20-5)	B		6.20	PAH	V
2.45	Pf (19-5)			7.60	PAH	V
2.47	Pf (18-5)	B			Huβ	
2.50	Pf (17-5)	B		7.80	PAH	V
2.53	Pf (16-5)	B		8.30	Uid	V
2.56	Pf (15-5)	B		8.60	PAH	V
2.63	Brβ	B		11.05	PAH	V
	Pf (14-5)			11.23	PAH	V
2.68	Pf (13-5)	B		12.40	Huα	V
2.75	Pf (12-5)	B		12.77	PAH	V
2.87	Pf (11-5)	B		13.15	PAH	V
3.00	H₂ ?			13.39	Uid	
3.04	Pfε	B		13.60	PAH	V
3.08	Uid			13.96	Uid	
3.23	H₂ ?			14.20	PAH	V
3.30	PAH	V		14.80	Uid	
	Pfδ			15.40	Uid	
3.40	meth. gr.			15.60	Uid	
3.43	Uid			16.40	PAH	V
3.47	Uid			17.05	H₂ ?	
3.64	Hu (19-6)			17.38	PAH	V
3.70	Hu (18-6)	B		17.70	Uid	
3.75	Hu (17-6)	B		17.86	[Fe II]	V
	Pfγ			18.60	fost.	
3.82	Hu (16-6)	B		18.70	[S III]	V
3.91	Hu (15-6)	B		19.05	fost.	
3.97	Uid			19.30	fost. + enst.	
3.99	Uid			25.99	[Fe II]	V
4.02	Hu (14-6)	B		26.00	fost., enst. bend	
4.05	Brα	B		29.40	Uid	V
4.11	Uid			29.60	Uid	
4.17	Hu (13-6)	B		31.00	fost.	
4.19	H₂ ?			31.20	Uid	
4.25	Uid			33.05	Uid	
4.44	Hu (12-6)	B		33.20	enst.	V
4.65	Hu (11-6)	B		33.50	[S III]	V
	Pfβ			33.55	fost.	
4.70	H₂ ?			34.50	enst. + diop.	
5.06	H₂ ?			34.80	[Si II]	V
5.13	Huδ	B		35.30	enst.	
5.23	PAH				[Fe II]	V

Notes. Ident. means the proposed feature identifications, enst. is enstatite, diop. is diopside, fost. is fosterite, meth. gr. is related to methil groups, and Uid means unidentified features. References (Ref.): B = Benedettini et al. (1998); V = Voors (1999). It is important to cite that except where noted, otherwise, the identifications are ours.

5.1 The effective temperature

The effective temperature values for CD-42°11721 found in the literature vary between 12 300 K (Hillenbrand et al. 1992) and 31 600 K (Cidale et al. 2001). Since in our spectra there is the presence of emission He I lines and the absence of He II lines, we can therefore conclude that the effective temperature must be in the range between 13 000 K (see Machado & de Araújo 2003) and 30 000 K.

IUE spectra have been used to constrain the spectral type of CD-42°11721 to early B (or B0) by Shore et al. (1990). This result should, however, be taken with caution, because: (i) CD-42°11721 lies in a crowded region with even some close-by X-ray sources (see

Hamaguchi et al. 2005), (ii) with an elliptical aperture with extensions of 10×20 arcsec², *IUE* observed definitely more than one star, and (iii) the *IUE* flux is much stronger and clearly offset from our optical spectrum, also indicating that multiple sources have been observed. The *IUE* spectrum can therefore not be used for a proper temperature determination and the classification as a B0 (or early B-type) star is therefore not justified.

The absence or presence of individual ionization stages of the metals identified in our spectrum (see Table A1) can be also used for a better restriction of the effective temperature. Inspecting the ionization potentials for the different ions with observed lines in our spectra, we can state that CD-42°11721 shows clear hints for the presence of ions with an ionization potential below $\chi \simeq 25\,\mathrm{eV}$ like, for example, C III, O II, N II, Ne II, He I recombination lines, and (even though very weak) S III. On the other hand, no lines from ions with ionization potential higher than ~27 eV could be identified. Good tracers for a higher ionization potential are the lines from Ar III, N III and Cl III as have been observed, for example, from the compact planetary nebula B[e] star Hen 2−90 (Kraus et al. 2005). From this narrow range between 25 and 27 eV, which is just above the He I ionization potential, we conclude that the effective temperature can only slightly exceed the value of 13 000 K (Machado & de Araújo 2003). In fact, in order to reproduce the shape of the optical continuum (which for a given extinction is strongly temperature sensitive, see Section 5.4), the effective temperature cannot exceed the value of about 15 000 K. We thus conclude that CD-42°11721 has an effective temperature of $14\,000 \pm 1000\,\mathrm{K}$.

5.2 The distance

The most controversial parameter of CD-42°11721 is its distance. Literature values range from 136 pc (Elia et al. 2004) over 160 pc (Hillenbrand et al. 1992) and 400 pc (de Winter & Thé 1990) up to 2 kpc (McGregor et al. 1988), 2.5 kpc (Lopes et al. 1992) and even 2.6 kpc (Shore et al. 1990). This range in distances by about a factor of 20 leads to a scatter in stellar luminosity by a factor of 400.

For the distance determination from our spectra we make use of the relations for the interstellar absorption lines of Na I and Ca II-K given by Allen (1973). From the equivalent widths of these lines (see Table A1) we find the following distances.

(i) $d = 1.23\,\mathrm{kpc}$ derived from the Na I lines, and
(ii) $d = 1.06\,\mathrm{kpc}$ derived from the Ca II-K lines.

Both values agree quite well and we will adopt the mean value of $d \simeq 1.15\,\mathrm{kpc}$, which lies between the very small and very large distances found in the literature, as a reasonable value. Based on the relations used, we can estimate the error in distance. Taking into account the errors in the measurements of the equivalent widths, of the order of 20 per cent, the error in distance results in 0.15 kpc. We are aware that this error does not reflect the full error, that might in principle be larger than this, since the distance estimated from the use of interestellar absorption lines contains a systematic error due to the statistical relations used. In our opinion, this parameter remains to be the worst estimated; consequently, all the conclusions that depend directly on it must be taken with caution.

5.3 The interstellar extinction

The extinction towards CD-42°11721 is believed to be quite high. Hints for this are provided by the strength of the interstellar diffuse feature at 4430 Å and the faint *IUE* SWP spectrum (Shore et al. 1990). Literature values for the visual interstellar extinction, A_V,

Table 4. Observed line ratios used for the extinction derivation.

n	Pa(n)/Hϵ	Pa(n)/Hδ	Pa(n)/Hγ
17	1.308	0.662	0.357
20	0.876	0.443	0.239
21	0.799	0.404	0.218
24	0.476	0.241	0.130

Table 5. Mean extinction values, A_V in magnitudes, from the line ratios calculated for different mass fluxes and electron temperatures. The Paschen lines used to calculate the mean values are Pa(17), Pa(20), Pa(21) and Pa(24).

		$F_{\rm m}$ (g s^{-1} cm^{-2})			
	$T_{\rm e}$ (K)	10^{-5}	10^{-6}	10^{-7}	10^{-8}
Pa(n)/Hϵ	12 000	5.065	4.775	4.476	4.398
Pa(n)/Hδ	12 000	4.960	4.571	4.298	4.276
Pa(n)/Hγ	12 000	5.153	4.688	4.493	4.521
Pa(n)/Hϵ	15 000	4.995	4.697	4.409	4.344
Pa(n)/Hδ	15 000	4.855	4.464	4.208	4.197
Pa(n)/Hγ	15 000	4.984	4.535	4.354	4.393
$\langle A_V \rangle$	12 000	5.059	4.678	4.422	4.398
$\langle A_V \rangle$	15 000	4.945	4.565	4.324	4.311

are found to range from 4.2 mag (Cidale et al. 2001) to 7.1 mag (de Winter & Thé 1990). With such an enormous range of extinction values, it is impossible to draw any reliable conclusion from our optical spectra. We therefore attempt to further constrain the extinction.

As a first attempt we tried to use the Pagel method (Pagel 1969). This method is based on a relation between the observed fluxes of Fe II forbidden lines and the reciprocal wavelengths. However, in the case of CD-42°11721, it could not be employed due to the lack of enough non-blended [Fe II] lines in our high-resolution spectra.

We therefore make use of the method suggested by Kraus (in preparation) that is based on the line ratios of the Paschen lines over the Balmer lines. The red edge of our FEROS spectrum shows the presence of well-resolved Paschen lines from Pa(10) up to Pa(40). In addition, on the blue edge of the spectrum, we observe the Balmer lines up to H9. The most unaffected line ratio to derive the extinction according to Kraus (in preparation) is the line ratio Pa(10)/H9. Since the FEROS data are not flux calibrated, we derive the line strengths by calibrating the data with the Cassegrain spectrum. This spectrum has, however, a narrower wavelength range than FEROS. We extrapolated the continuum of the Cassegrain spectrum to the blue and red edges of FEROS, but the lines in these ranges have a much larger uncertainty and are therefore not so useful to derive the reddening. We therefore concentrate on the line ratios Pa(n)/Hϵ, Pa(n)/Hδ, Pa(n)/Hγ with $n = 15, \ldots, 25$. The reasons for these restrictions are the following.

(i) Paschen lines from levels higher than $n = 25$ are weak and a proper determination of their line strengths becomes difficult.

(ii) Paschen lines from levels lower than $n = 15$ suffer from the uncertain continuum extrapolation beyond the red edge of the Cassegrain spectrum.

(iii) The H9 line is affected by the uncertain continuum extrapolation of the Cassegrain spectrum which has a rather noisy continuum at the blue edge.

(iv) The H8 line is not useful since it is blended with an He I line.

Restricting to unblended, clearly resolved Paschen lines (see Fig. 1) reduces the lines suitable for a proper extinction determination to Pa(17), Pa(20), Pa(21) and Pa(24). For these lines the observed line ratios with the Balmer lines Hϵ, Hδ and Hγ are summarized in Table 4.

To determine the extinction, we need to know (at least approximately) the electron temperature in the wind and the mass flux of the star. With an effective stellar temperature of about 15 000 K and the fact that in a stellar wind the Paschen lines form very close to the central star where the wind temperature is still rather high, we use the unreddened line ratios for the two different electron temperatures, 12 000 and 15 000 K. The mass flux of the star is not known a priori. However, since the different line ratios should result in the same (or a very similar) extinction value, we can exclude the very high mass fluxes (i.e. $F_{\rm m} \geqslant 10^{-4}$ g s^{-1} cm^{-2}) in the tables of Kraus

(in preparation), because they result in a large spread in extinction values.

To pin down the extinction, we first calculate a mean value of the different line ratios found for each mass flux in the range $F_{\rm m} = 10^{-5}$–10^{-8} g s^{-1} cm^{-2} and for the two different electron temperatures. These mean values are given in Table 5. From this table it is clear already, that the visual extinction must be in the range from 4.3 to 5.0 mag, which is in rough agreement with the values of 4.2 and 4.3 mag found by Cidale et al. (2001) and Hillenbrand et al. (1992), and the value of about 5 mag given by McGregor et al. (1988).

To restrict the extinction even further, we next calculate the recombination line luminosities of the Paschen lines, using the model parameters for $T_{\rm e}$ and $F_{\rm m}$, redden them with the corresponding extinction value found, and compare them with the observed line luminosities under the assumption of a distance of 1.15 kpc. Such a comparison can give only a rough result, because the line luminosities, different from the line ratios, do depend on individual stellar parameters like the stellar radius and mass-loss rate. Assuming spherical symmetry, which should result in a lower limit of the real mass flux of the star, and varying the stellar parameters in a reasonable range, we found that even with this rough method we can exclude the mass fluxes lower than 10^{-6} g s^{-1}cm^{-2}. This means that the extinction towards CD-42°11721 is of the order of 4.8 ± 0.2 mag.

5.4 Stellar radius and luminosity

The stellar radius of CD-42°11721 can be found by fitting the Cassegrain spectrum with classical Kurucz model atmospheres (Kurucz 1979). Since the effective temperature of the star is in the range 13 000–15 000 K, we fitted Kurucz model atmospheres for stars with solar metallicity and different log g values, reddened with 4.8 ± 0.2 mag interstellar extinction. From these fittings it turned out that no reliable fit was found for $A_V = 5.0$ mag, while for the values of $A_V = 4.6$–4.8, especially the models with low to mid surface gravity, fitted best (Fig. 7). From the fitting parameter which is simply R_*^2/d^2 and for a distance of 1.15 ± 0.15 kpc we can derive the stellar radius. This has been done for all the best-fitting model atmospheres. The resulting stellar radius taking into account the error in distance is $R_* = 17.3 \pm 0.6$ R$_\odot$. We want to stress that this is an upper limit for the stellar radius, because the optical continuum might contain some contributions from free–free and free–bound emission generated in the wind. Nevertheless, the contribution of the wind can only be of minor impact because the photometric data in the near-IR do not show influences of free–free emission (see
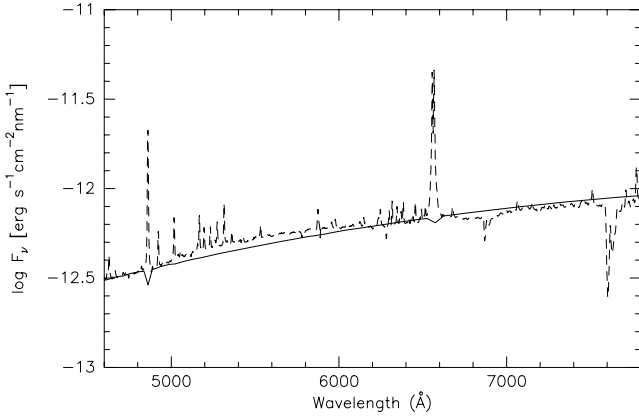
Figure 7. Fitting of the observed optical continuum (dashed line) with Kurucz model atmospheres (solid lines, Kurucz 1979). Shown is one of the best fits achieved for a solar metalicity star with $T_{\mathrm{eff}} = 14\,000$ K, $\log g = 3.0$, and a foreground extinction of $A_V = 4.8$ mag.

Table 6. Stellar parameters for CD-42°11721 found from our high-resolution optical spectra as described in Section 5. The mass and $\log g$ values have been derived under the assumption that CD-42°11721 is a post-main-sequence object. The values in the second row represent the error in each measurement.

T_{eff} (K)	R_* ($R_{\odot}$)	L_* ($L_{\odot}$)	M_{initial} ($M_{\odot}$)	$\log g$	d (kpc)	A_V (mag)
14 000	17.3	1.0×10^4	8–10	~3	1.15	4.8
±1000	±0.6	$\pm0.3 \times 10^4$			±0.15	±0.2

Section 6.1). We therefore regard the derived ~17 $R_{\odot}$ as a reasonable value for the stellar radius. Since we know the radius and the effective temperature, we could find a stellar luminosity of $L_* = (1.0 \pm 0.3) \times 10^4 \, L_{\odot}$.

To finish our optical analysis, we summarize in Table 6 the stellar parameters of CD-42°11721 derived within this section.

6 MODELLING OF THE SPECTRAL ENERGY DISTRIBUTION OF CD-42°11721

To construct a proper SED for CD-42°11721, we collected all photometric data available in the literature and listed them in Table 7. There, the observed wavelengths (Column 1), the measured fluxes (Column 2), the aperture diameters (Column 3), and the references (Column 4) are given. As can be seen in Fig. 8, considering all data and different apertures, the SED is double-peaked, similar to those HAeBe stars called 'group I' (Meeus et al. 2001), though differently than other objects of this group, its first peak is shifted to higher wavelengths, around 2 μm. However, as cited in Section 4, the data from observations with large apertures are contaminated by the reflection nebula and other sources and do not come from the star itself. Based on this, we have decided to consider in our modelling only data with aperture diameters equal or smaller than 15 arcsec. It is important to cite that the most confident results would be obtained from the modelling of an SED considering only photometric data using apertures around 1 or 2 arcsec; however, there is not enough available data to build a reliable SED for this object.

In this section, we present the modelling of the SED of CD-42°11721, using three diferent codes, that solve the problem of radiative transfer in a circumstellar dust medium, considering three

Table 7. Photometric data of CD-42°11721 available in the literature.

Wavelength (μm)	Flux (W m^{-2} μ m^{-1})	Aperture diameter[a] (arcsec)	References
0.36	4.67×10^{-13}	15.0	1[b]
0.36	3.86×10^{-13}	9–13	2
0.44	6.23×10^{-13}	15.0	1[b]
0.44	5.44×10^{-13}	9–13	2
0.56	1.16×10^{-12}	21.5	1[b]
0.56	1.07×10^{-12}	15.0	1[b]
0.56	9.22×10^{-13}	9–13	2
0.64	2.17×10^{-12}	15.0	1[b]
0.79	2.66×10^{-12}	15.0	1[b]
1.23	3.69×10^{-12}	15.0	3
1.25	4.40×10^{-12}	13.0	1[b]
1.25	3.92×10^{-12}	8.0	2MASS
1.63	5.11×10^{-12}	15.0	3
1.65	5.37×10^{-12}	13.0	1[b]
1.65	4.81×10^{-12}	8.0	2MASS
2.19	6.60×10^{-12}	15.0	3
2.20	7.11×10^{-12}	13.0	1[b]
2.20	6.33×10^{-12}	8.0	2MASS
3.30	6.50×10^{-12}	14 × 20	*ISO*-SWS
3.40	6.49×10^{-12}	14 × 20	*ISO*-SWS
3.45	8.31×10^{-12}	13.0	1[b]
3.50	6.29×10^{-12}	14 × 20	*ISO*-SWS
3.79	5.83×10^{-12}	15.0	3
4.29	6.86×10^{-12}	18.3	MSX
4.35	6.89×10^{-12}	18.3	MSX
4.64	4.87×10^{-12}	15.0	3
4.80	4.37×10^{-12}	13.0	1[b]
6.20	3.23×10^{-12}	14 × 20	*ISO*-SWS
7.70	2.24×10^{-12}	14 × 20	*ISO*-SWS
8.28	3.26×10^{-12}	18.3	MSX
8.38	1.73×10^{-12}	15.0	3
8.60	1.77×10^{-12}	14 × 20	*ISO*-SWS
9.69	9.06×10^{-13}	15.0	3
9.70	1.26×10^{-12}	14 × 20	*ISO*-SWS
11.00	1.14×10^{-12}	14 × 20	*ISO*-SWS
12.00	1.98×10^{-12}	45.0×270.0	*IRAS*
12.00	9.26×10^{-13}	80.0	4
12.13	1.54×10^{-12}	18.3	MSX
12.89	4.90×10^{-13}	15.0	3
14.65	6.47×10^{-13}	18.3	MSX
21.34	7.84×10^{-13}	18.3	MSX
25.00	1.21×10^{-12}	45.0×276.0	*IRAS*
25.00	6.68×10^{-13}	80.0	4
60.00	1.60×10^{-12}	90.0×282.0	*IRAS*
60.00	1.31×10^{-12}	80.0	4
100.00	6.63×10^{-13}	180.0×300.0	*IRAS*
100.00	5.12×10^{-13}	80.0	4
350.00	2.32×10^{-16}	18.5	5
450.00	8.02×10^{-17}	18.3	5
600.00	1.11×10^{-17}	17.5	5
750.00	4.74×10^{-18}	18.0	5
800.00	5.06×10^{-18}	17.0	5
850.00	2.86×10^{-18}	18.0	5
1100.00	6.20×10^{-19}	18.8	5
1300.00	4.58×10^{-19}	19.8	5
1300.00	4.79×10^{-19}	28.0	6

different scenarios, for example, a spherically symmetric geometry, a passive flared disc and an outflowing disc wind. We aim to determine which scenario describes better the SED of this star, assuming the set of stellar parameters obtained from our optical analysis. Our codes that represent the flared disc and the outflowing disc wind scenario are presented here for the first time.

Table 7 – *continued*

Wavelength (μm)	Flux (W m^{-2} μm^{-1})	Aperture diameter^a (arcsec)	References
1300.00	7.54×10^{-19}	23.0	7
36000.00	3.06×10^{-24}	2.5	8

References: 1 = de Winter & Thé (1990); 2 = Herbst (1975); 3 = Berrilli et al. (1992); 4 = Elia et al. (2005); 5 = Mannings (1994); 6 = Hillenbrand et al. (1992); 7 = Henning et al. (1994); 8 = Skinner, Brown & Stewart (1993); *ISO*-SWS = Acke & van den Ancker (2004); MSX = Egan et al. (1999); *IRAS* = http://irsa.ipac.caltech.edu/IRASdocs/iras_mission.html; 2MASS = http://www.ipac.caltech.edu/2mass/releases/allsky/doc/sec1_6b.html.

^{a} = except by *IRAS* and *ISO*-SWS, that have rectangular apertures.

^{b} = mean values of observations with same aperture and from the same reference.
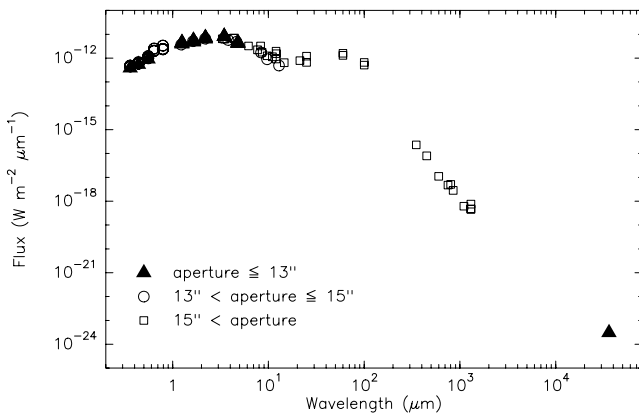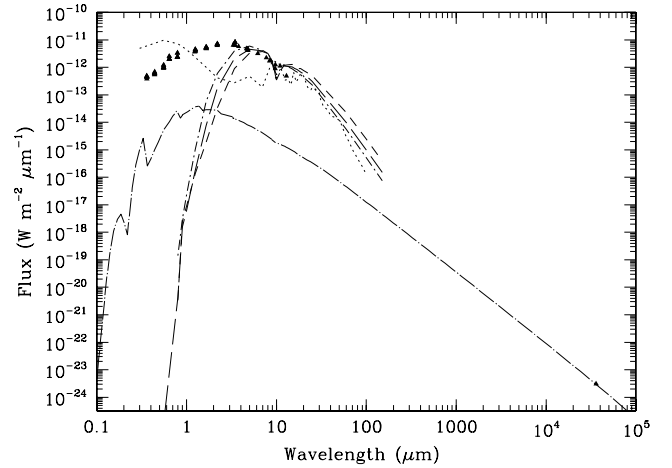

Figure 8. The SED of CD-42°11721, considering all data with different apertures presented in Table 7.

6.1 Free–free and free–bound emission

For the modelling of the SED of CD-42°11721, our first step was to determine the contribution of the free–free and free–bound emission (hereafter ff-fb emission) to the total continuum. The ff-fb continuum can be calculated by accounting for the observed 3.6 cm emission that was obtained with an aperture size of 2.5 arcsec (see Table 7) and that can be ascribed purely to the ionized wind material. Since we do not know exactly the wind geometry and the possible inclination under which the system of CD-42°11721 is seen, we calculated the ff-fb continuum assuming an isothermal ($T_e = 10\,000$ K) spherically symmetric wind, with an outer edge of 1500 au. The mass-loss rate needed to fit the 3.6 cm emission ($\dot{M} = 2.86 \times 10^{-6}$ M$_\odot$ yr^{-1}) must be considered as a lower limit. The terminal velocity, which is proportional to the escape velocity on the stellar surface, was calculated from the stellar parameters given in Table 6 and it is 515 km s^{-1}. It turns out that the contribution of the ff-fb continuum is negligible in the optical and near-IR spectral range (see Fig. 9).

6.2 Spherically symmetric envelope

Our optical results revealed that the circumstellar scenario of CD-42°11721 should probably be composed of a non-spherical geom-

Figure 9. Different models reproducing the SED of CD-42°11721, considering a spherical symmetric envelope. We can see model A (dashed line), model B (long-dashed line), model C (dot–short dashed line) and model D (dotted line). A detailed explanation of these models can be seen in the text and also in Table 8. The triangles represent the photometric data obtained in the literature. The dot–long-dashed line is the ff-fb emission that fits the 3.6-cm data point. Its contribution, as can be seen, to the IR part of the SED is negligible.

etry. However, for the sake of completeness, we modelled the SED of this star considering also a circumstellar spherically symmetric dust envelope.

Our numerical treatment of radiative transfer in a spherical envelope was described in Lorenz-Martins & Pompéia (2000). The Monte Carlo scheme is used for representing the propagation of radiative energy photon by photon. For each interaction between a 'photon' and a grain, a fraction of the energy is stored (absorption) and the remaining part is scattered according to the scattering diagram. Two species of grains are used and they interact with each other. The stellar radiation leads to a first distribution of dust temperature and the thermal radiation from grains is simulated, giving after several iterations the equilibrium temperature. Here two species of grains are considered both with a numerical density decreasing as r^{-2}, which corresponds to an expansion at constant velocity. The grains can be present at the same or at different distances of the central star. The following physical quantities are required in a first guess and are subsequently fixed by fitting the IR/near-IR flux: the effective temperature of the central star, $T_{\rm eff}$; grain sizes and refractive indices for all wavelengths; the extinction opacity, $\tau_{\rm ext}$ at $\lambda = 9$ μm; the inner radii of the dust envelope (say, $R_{\rm Sil}$, inner radius for amorphous silicate grains; $R_{\rm Crys}$, inner radius for crystalline silicate grains, or $R_{\rm AC}$ amorphous carbon grains), and $R_{\rm o}$ the outer radius of the dust envelope.

The models give the spectral repartition not only of the total flux but also of its different components (direct, scattered, thermal for each species of grain), as well as the angular distribution of these radiation fields and the radial dependence of dust temperatures. The absorption and scattering efficiencies, as well as the albedo for the grains were calculated by us using the Mie theory and the optical constants given by Rouleau & Martin (1991), David & Pégourié (1995) and Jaeger et al. (1998).

Several models, considering different sets of parameters, including those derived by our optical analysis, were calculated by us. The results of four of them are presented in Table 8. There, the name of

Table 8. Results of the modelling considering a spherical symmetric envelope. The temperatures are given in K. More details are in the text.

Model	T_{eff}	T_{AC}	T_{Sil}	T_{Crys_1}	T_{Crys_2}
A	10 000	564	364	–	–
B	15 000	781	570	–	–
C	25 000	1038	880	–	–
D	10 000	–	–	346	327

each model (Column 1) is followed by T_{eff} (in K, Column 2) and the temperatures (also in K) of the hottest grains (Columns 3, 4, 5 and 6). Other parameters are kept constant in these models. These are $\tau_{ext} = 3.0$ at $\lambda = 9$, $R_{Sil} = R_{Crys} = R_{AC} = 200\,R_*$ and $R_o = 5000R_*$. The grains sizes are also fixed at 200 Å and the ratio of amorphous carbon over amorphous silicate grains is set to 0.50 and the ratio of crystalline silicate grains needed in model D is also set to 0.5.

As can be seen in Fig. 9, the total SEDs (including the stellar and dust contributions) obtained by us, assuming a spherical geometry for the dust envelope, could not model properly the SED of CD-42°11721, especially the optical region. Models A and D differ one from the other only by the dust species (see Table 8). In model A we have used amorphous silicates and amorphous carbon grains simultaneously, while in model D we have considered only crystalline silicates. The other two models (B and C) differ from the model A only by T_{eff} as can be seen in Table 8. These models present very similar fitting, even considering quite different set of parameters.

6.3 Equatorial disc

Based on our optical analysis, a more complex circumstellar geometry, most plausibly a disc scenario, seems to be indeed necessary to account for the observed SED of CD-42°11721.

The presence of a disc seems to be the better answer to explain the spectral characteristics of not only B[e] supergiants (Zickgraf et al. 1985), but also HAeBe stars. The discs around young stars are detected with millimetre interferometry (Mannings & Sargent 1997, 2000; Fuente et al. 2004), and in some cases, they are visible in optical images of the stars, either via scattered light or in silhouette against a background light source (Burrows et al. 1996; McCaughrean & O'Dell 1996; Grady et al. 2000).

Due to the absence of images and also interferometric observations for CD-42°11721, we have decided to reproduce its SED considering two different types of discs, one typical of HAeBe stars and another one, typical of B[e]sg stars.

6.3.1 Passive flared disc

Considering CD-42°11721 as an HAeBe star, we need to assume the existence of a passive equatorial disc, where passive means that the disc is heated purely by stellar irradiation.

Specifically for CD-42°11721, we need to explain the location of the hot dust that might be responsible for the peak seen in its SED. We are assuming here that the hot dust is located at the surface of the circumstellar disc. For the surface to become much hotter than the interior, it must be inclined with respect to the infalling stellar radiation, that is, the disc must be flared. Such a flaring can happen naturally when the disc is in hydrostatic equilibrium in vertical
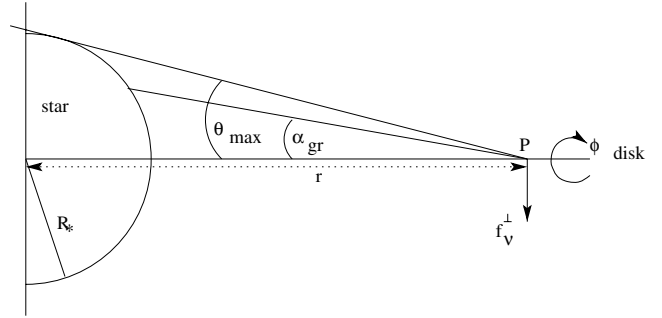
Figure 10. Sketch of stellar illumination of a razor-thin disc. The grazing angle α_{gr} (see the text for details) is also indicated.

direction with a radial temperature distribution that falls off more slowly than r^{-1} (Kenyon & Hartmann 1987).

The flared disc is proposed to explain the spectral characteristics of young pre-main-sequence stars of 'group I' (Meeus et al. 2001; Dullemond & Dominik 2004; Acke et al. 2005). The geometry of this kind of disc also explains the presence of a more intense flux in the far-IR, seen in HAeBe stars of 'group I', since the most distant regions in the disc surface receive a higher amount of stellar radiation (they see a larger solid angle of the star). This kind of disc can also explain the presence of the 'dual-dust' chemistry, since the PAH molecule emission would be formed in the surface layers of the disc and the silicate bands in the inner regions of it, closer to the star (Meeus et al. 2001; Dullemond & Dominik 2004). However, as cited in Section 4, in the case of CD-42°11721, this mixed chemistry probably does not belong to the CSM of this star.

Considering a flared disc scenario, we developed an analytical two-layer model that contains an optically thick ($\tau_V^{mid} \gg 1$) mid-layer which is isothermal in z-direction. The mid-layer is sandwiched by two top layers which are marginally optically thick at visual wavelengths but still optically thin at IR wavelengths, that is, $\tau_V^{top} \gg 1$ and $\tau_{IR}^{top} \leqslant 1$. Consequently, the infalling stellar light is completely absorbed within the top layer. The dust particles re-radiate the energy at IR wavelengths, so half the redistributed energy leaves the disc into space, and the other half penetrates the mid-layer and heats it. As a third distinct region we define the disc photosphere which encloses the uppermost part of the top layer and whose location is defined by the parameter h (see below).

Further, we make the following assumptions. The disc is in hydrostatic equilibrium in z-direction, gas and dust are well mixed throughout the disc, and in the mid-layer gas (g) and dust (d) are in thermal equilibrium at the same temperature $T_g = T_d = T_{mid}$. The emission and absorption of the gas component is ignored.

In addition, our (gas) disc extends down to the stellar surface with no inner hole. The existence of such a hole would lead to a puffed-up inner rim and self-shadowing effects of the disc (see Dullemond, Dominik & Natta 2001; Dullemond 2002).

For a razor-thin passive disc (see Fig. 10) around a star with effective temperature T_* and radius R_* the monochromatic flux entering the disc perpendicular to the surface at a distance r from the star is

$$f_\nu^\perp = \int_0^\pi \int_0^{\theta_{max}} B_\nu(T_*) \sin^2 \theta \sin \phi \, d\theta \, d\phi$$

$$= B_\nu(T_*) \left[\arcsin \frac{R_*}{r} - \frac{R_*}{r} \sqrt{1 - \left(\frac{R_*}{r} \right)^2} \right] \quad (1)$$
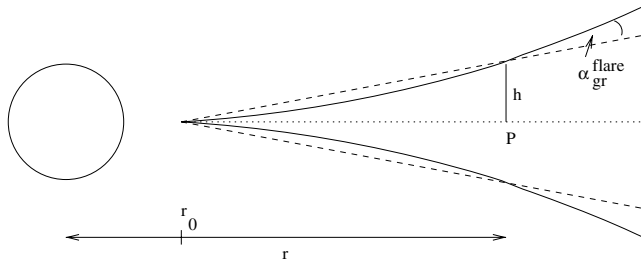
Figure 11. Sketch of a flared disc. The flaring term of the grazing angle is indicated. The inner radius of the dust disc is r_0.

with

$$\theta_{max} = \arccos\left(\sqrt{1 - \left(\frac{R_*}{r}\right)^2}\right). \tag{2}$$

We assume that the star emits a Planck spectrum. At distances large compared with the stellar radius, this relation reduces to

$$f_\nu^\perp \xrightarrow{r \gg R_*} B_\nu(T_*)\frac{2}{3}\left(\frac{R_*}{r}\right)^3. \tag{3}$$

The flux can be parametrized in terms of the solid angle Ω under which the star is seen from a disc surface element at a distance r and the so-called grazing angle α_{gr}, that is, the mean angle of incidence of the stellar flux

$$f_\nu^\perp = \alpha_{gr}\Omega B_\nu(T_*). \tag{4}$$

The grazing angle of a razor-thin disc is therefore

$$\alpha_{gr}^{razor} = \frac{1}{\Omega}\left[\arcsin\left(\frac{R_*}{r}\right) - \frac{R_*}{r}\sqrt{1 - \left(\frac{R_*}{r}\right)^2}\right], \tag{5}$$

which for large distances reduces to the handy formula first introduced by Chiang & Goldreich (1997):

$$\alpha_{gr}^{razor} \xrightarrow{r \gg R_*} \frac{4}{3\pi}\frac{R_*}{r} \simeq 0.4\frac{R_*}{r}. \tag{6}$$

This relation also holds for a wedge-shaped disc as long as its opening angle is small.

In a flared disc the surface is curved and the grazing angle increases with distance from the star (see the solid lines in Fig. 11). Therefore, the flared disc intercepts more stellar light and is heated more efficiently. The grazing angle of the flared disc is by the amount α_{gr}^{flare} higher than for a flat disc (Fig. 11). This flaring term of the grazing angle can be computed from

$$\alpha_{gr}^{flare} = \arctan\frac{dh}{dr} - \arctan\frac{h}{r} \simeq r\frac{d}{dr}\left(\frac{h}{r}\right) \tag{7}$$

and the total grazing angle becomes simply

$$\alpha_{gr} = \alpha_{gr}^{razor} + \alpha_{gr}^{flare}. \tag{8}$$

With this new grazing angle, which is a function of $h(r)$, that is, the bottom of the photosphere or half the thickness of the disc, we can calculate the flux penetrating the flared disc in z-direction.

The photosphere encloses the uppermost part of the top layer. Its onset is described by the parameter h, which is defined as the height z above the mid-plane where the visual optical depth along the direction of the infalling stellar light, that is, along the grazing angle, equals 1. This leads to a vertical optical depth of

$$\tau_V^\perp = \sin\alpha_{gr}. \tag{9}$$

Since the disc is assumed to be in hydrostatic equilibrium, $\tau_V^\perp$ can be calculated as

$$\tau_V^\perp = \kappa_V\rho_0(r)\int_h^\infty e^{-(z^2/2H^2)}\,dz, \tag{10}$$

where ρ_0 is the density in the mid-plane and H is the scaleheight of the disc given by

$$H = \sqrt{\frac{kT}{GM_*\mu m_H}}\,r^{3/2}. \tag{11}$$

By equaling equations (9) and (10) h can be determined, but it is a function of temperature and grazing angle.

The downward- and upward-directed fluxes, $F^\downarrow$ and $F^\uparrow$, are in equilibrium throughout the passive disc. We can calculate these two fluxes explicitly at the boundary between the isothermal mid-layer and the top layer. All infalling stellar radiation is reprocessed within the top layer. We assume that half the incident stellar flux is re-radiated into space and the other half penetrates the mid-layer. The downward-directed flux becomes

$$F^\downarrow = \frac{1}{2}f^\perp = \frac{1}{2}\int\alpha_{gr}\Omega B_\nu(T_*)\,d\nu \tag{12}$$

and the flux leaving the mid-layer in upward direction is

$$F^\uparrow = 2\pi\iint B_\nu(T_{mid})(1 - e^{-\tau_\nu/\mu})\mu\,d\mu\,d\nu, \tag{13}$$

where T_{mid} is the isothermal temperature of the mid-layer, and we set $\mu = \cos\theta$ with θ as the angle measured from the z-axis. The visual optical depth of the mid-layer in vertical direction can be written in the form

$$\tau_V^{mid}(r) = \tau_V^{mid}(r_0)\left(\frac{r}{r_0}\right)^{-s}, \tag{14}$$

with the visual optical depth at the inner edge, $\tau_V^{mid}(r_0)$, and the exponent s as free parameters, and the optical depth at frequency ν is simply

$$\tau_\nu = \tau_V\frac{\sigma_\nu^{ext}}{\sigma_V^{ext}}, \tag{15}$$

where σ^{ext} is the dust extinction cross-section. The temperature of the mid-layer, T_{mid}, follows from equaling equations (12) and (13). This temperature is, however, a function of the grazing angle.

We have now three important parameters, α_{gr}, h and T_{mid}, but none of them can be computed independently, instead they must be calculated iteratively.

We have to specify the visual optical depth in the top layer in z-direction, τ_V^{top}. It should be high enough so that first, the infalling stellar radiation is completely absorbed and, secondly, the dust grains at the bottom of the top layer reach a temperature close to that of the mid-layer in order to guarantee a smooth transition. On the other hand, τ_V^{top} must be small enough to allow the dust emission, which occurs at IR wavelengths, to escape the top layer.

The radiation transfer equation of a plane-parallel slab is

$$I_\nu(\mu, \tau_\nu) = I_0\,e^{\tau_\nu/\mu} - \int S_\nu(t)\,e^{-(t-\tau_\nu)/\mu}\frac{dt}{\mu}, \tag{16}$$

with the source function S_ν, the incident intensity I_0 and $\mu = \cos\theta$. The radiation transfer equation is split into upstreams, I_ν^+, that penetrate the top layer from the mid-layer, and downstreams, I_ν^-, that cross the top layer starting from the surface. The incident intensity is either the stellar radiation for downward-directed streams (but only for angles θ under which the star can be seen, else it is zero),

or the emission of the mid-layer, $B_\nu(T_{\mathrm{mid}})(1 - \mathrm{e}^{-\tau_\nu^{\mathrm{mid}}/\mu})$, for the upward-directed streams.

With the help of the Feautrier parameters

$$u_\nu = \frac{1}{2}\,(I_\nu^+ + I_\nu^-), \tag{17}$$

$$\upsilon_\nu = \frac{1}{2}\,(I_\nu^+ - I_\nu^-), \tag{18}$$

the mean intensity J_ν becomes

$$J_\nu = J_\nu(\tau_\nu) = \int u_\nu(\mu, \tau_\nu)\,\mathrm{d}\mu, \tag{19}$$

which is needed to calculate the source function and the emission of the grains. The source function itself determines the upstream and downstream of the intensity which leads to an iterative calculation of the radiation field.

Finally, the temperature of the grains at each location in the top layer follows from balancing their absorption from the surrounding radiation field, J_ν, and their emission at their equilibrium temperature, T_{d}.

In our code, we are adopting a mixture of spherical silicates and amorphous carbon grains which follow the MRN (Mathis, Rumpl & Nordsieck 1977) grain size distribution. The particle sizes range from $a_{\mathrm{min}} = 75\,\text{\AA}$ to $a_{\mathrm{max}} \simeq 1\,\mu\mathrm{m}$. The absorption efficiencies of the dust particles are calculated with the Mie theory for spherical particles and scattering of the stellar light within the top layer is included.

For the modelling of CD-42°11721, assuming a flared disc scenario, we have used the physical parameters obtained by our optical analysis (extinction, effective temperature, distance, and luminosity) and the ff-fb emission (see Section 6.1). We keep the top layer optical depth fixed ($\tau_V^{\mathrm{top}} = 2$) and use a stellar mass of 8–10 $\mathrm{M}_\odot$ (see Section 7).

Considering this set of input parameters, the code calculates the location of the inner edge of the dust disc, which is defined by the dust evaporation temperature and may vary for different input values, especially of the optical depth of the mid-layer (i.e. the surface density distribution). Having fixed the inner edge of the disc, the disc structure and temperature distribution in vertical direction are calculated. Of special importance is thereby that the grain temperatures of the different grain sizes and dust components adapt to the isothermal temperature of the mid-layer. The dust SED is then calculated by integrating the emerging dust emission over the disc size.

The most serious boundary condition in our calculations is the request of an optically thick mid-layer, justifying the application of a flared disc. Intending to fulfill this condition and to reproduce the observed dust emission, we need to play mainly with the outer edge of the dust disc (r_{out}), the mid-layer optical depth at the inner edge of the dust disc [$\tau_V^{\mathrm{mid}}(r_0)$], and the exponent ($s$). Assuming values of s higher than 1.5, we obtain that only very small discs ($r_{\mathrm{out}} \leqslant 25\,\mathrm{au}$) can keep the mid-layer optically thick; however, in these cases, the dust disc emission is lower than the observed one. On the other hand, assuming $s = 1$ or 1.5, the density distribution is less steep and we can satisfy the mid-layer optical depth condition for larger discs and, consequently, the dust emission is better reproduced. We can also get good results assuming $\tau_V^{\mathrm{mid}}(r_0)$ in the range 2.5×10^2–4×10^3. Concerning the r_{out}, it is limited by the mid-layer optical depth condition.

The total SED is formed by the stellar, ff-fb and dust disc emission contributions. The stellar contribution is determined by the stellar parameters, especially the effective temperature and also the foreground extinction, obtained by our optical analysis. In panel (a) of
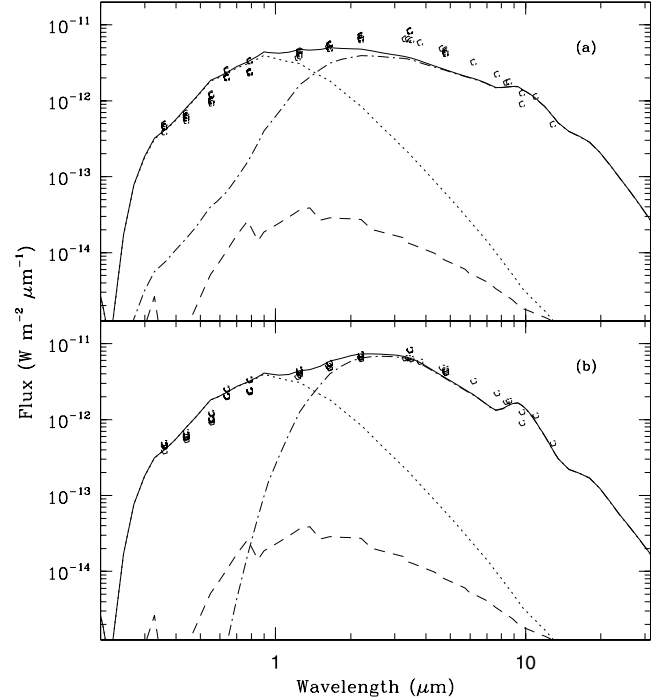

Figure 12. Modelling the SED of CD-42°11721, considering in panel (a) a flared disc scenario and assuming a less-steep density profile ($s = 1$). As can be seen, the observations cannot be well reproduced, because the near-IR emission is clearly underestimated. Panel (b) shows our best model considering the presence of an outflowing disc wind. The models were obtained assuming a disc seen with an inclination angle from 0° (pole-on) to 70°. The circles represent the photometric data obtained in the literature. The dotted line represents the stellar contribution; the dashed line, the ff-fb emission; the dot–dashed line, the dust disc contribution and the solid line, the total emission.

Fig. 12 we present our best result. It clearly shows deviations compared to the observations, especially the near-IR part that cannot be well fitted by our calculations. In this model, we are considering a fixed density profile with $s = 1$, $r_0 = 0.5\,\mathrm{au}$, $r_{\mathrm{out}} = 60\,\mathrm{au}$, and $\tau_V^{\mathrm{mid}}(r_0) = 2.5 \times 10^2$. On the other hand, an increase in the mid-layer optical depth (i.e. an increase in surface density) has caused an increase in far-IR flux and, consequently, it cannot be adjusted to the observations.

It is important to cite that the inclination angle of the disc, seen by the observer, is also an input parameter of our code and we have found that there is no difference in our model results, as long as we consider discs with inclination angles smaller than 70° (0° means pole-on). For larger inclination angles it is impossible to get a reasonable fit at all.

6.3.2 Outflowing disc wind

We have alternatively supposed the disc around CD-42°11721 to be an outflowing disc wind, typically ascribed to B[e] supergiants, where the dust would be uniformly distributed in it. Our code, for simplification, assumes that the disc is isothermal in z-direction, with a constant outflow velocity and a surface density described by

$$\Sigma(r) = \int_{-h}^{h} \rho(r,z)\mathrm{d}z = 2\int_0^h \rho(r,z)\,\mathrm{d}z, \tag{20}$$

where h is the height of the disc at a distance r, considering a constant opening angle for it, and $\rho(r,z)$ is the density distribution, being

derived according to the mass continuity equation

$$\rho(r, z) = \frac{\dot{M}}{4\pi(r^2 + z^2)v_\infty}. \tag{21}$$

Inserting this equation into equation (20), it follows that

$$\Sigma(r) = \Sigma_0 \left(\frac{r}{r_0}\right)^{-1} = \Sigma_0 \left(\frac{r_0}{r}\right) \tag{22}$$

with

$$\Sigma_0 = \frac{\dot{M}\alpha}{4\pi r_0 v_\infty} \tag{23}$$

and α is here the opening angle of the outflowing disc and r_0 is the dust sublimation radius. Equation (22) represents the surface density of the gas component. To convert it into the surface density of the dust component, we consider the gas-to-dust ratio, that is a factor of 100. For the temperature distribution we assume a power law of the form

$$T(r) = T_0 \left(\frac{r}{r_0}\right)^q, \tag{24}$$

where T_0 is the dust sublimation temperature, fixed at 1500 K.

We use the same grain size distribution and grain composition as for the flared disc. The model output is then the integrated flux of the star plus disc system, with the stellar parameters taken from our optical analysis, and reddened with the foreground extinction. The inclination angle of the star–disc system is a free input parameter.

The exponent of the temperature distribution (q, see Equation 24) is found to be the parameter with most severe influence on the resulting SED. We have obtained good results assuming different values of q in the range from 0 to -2. For values higher than -0.4, we could get good results, assuming quite low disc mass-loss rates ($\dot{M}_{\rm disc} \leqslant 10^{-7} \, {\rm M}_\odot \, {\rm yr}^{-1}$); however, the main problem in this case is that the temperature continues still high far away from the central star, what is not expected. On the other hand, using $q \leqslant -0.5$, it is necessary to have very high disc mass-loss rates ($\dot{M}_{\rm disc} \geqslant 10^{-4} \, {\rm M}_\odot \, {\rm yr}^{-1}$) or even large disc opening angles ($\alpha \geqslant 40°$) to reproduce the observed SED.

Panel (b) of Fig. 12 shows our best result, considering the following parameters: $\alpha = 20°$, $r_{\rm out} \geqslant 20 \, {\rm au}$, $\dot{M}_{\rm disc} = 8.7 \times 10^{-5} \, {\rm M}_\odot \, {\rm yr}^{-1}$ and $q = -0.4$. This result seems for us better than those obtained assuming a flared disc scenario. Regarding the outer edge of the disc ($r_{\rm out}$), we can get the same good results, assuming $r_{\rm out}$ with values from 20 to 8000 au (which corresponds to approximately the size of the aperture considered). This means that the disc is not optically thick anymore just after few au of distance from the star and the contribution from the optically thin region is negligible for the SED. This conclusion is in agreement with the fact that we can model the SED assuming a disc seen pole-on or with inclination angles lower than 70°, meaning that whole emission region is seen under these angles. Another interesting point is that our models are obtained assuming values of disc mass-loss rate that are in perfect agreement with those proposed for discs of B[e] supergiants. Another parameter that also influences our models is the terminal velocity of the disc wind (a decrease in v_∞ causes an increase in the dust disc emission); however, based on our optical observations (see Table 1), we decide to keep it fixed, $v_\infty = v_{\rm exp} = 60 \, {\rm km \, s}^{-1}$.

6.4 Discussion: model results

In the case of CD-42°11721 several works have tentatively described its SED using different codes and approaches. Hillenbrand et al. (1992) suggested that the SED of this star shows no evidence of a spherically symmetric envelope. According to these authors, the SED could be described by a flat, optically thick massive accretion disc. These discs present an optically thin region within the inner few stellar radii. These optically thin 'holes' would imply the absence of warm dust which would contribute with strong excess of emission in the near-IR region and that is seen in the SED of CD-42°11721. However, they did not treat the radiative transfer problem and their fits are not good, even at 3 μm. Natta et al. (1993) calculated models to CD-42°11721 taking the radiative transfer into account. Their model was solved considering a spherically symmetric dust envelope which would reprocess the radiation of the central source. The difference in this work is that they adopted a central source composed of a star and a circumstellar disc. In addition, they modified the dust properties at $\lambda > 100 \, \mu$m in order to match the observed submillimetre fluxes. Anyway, the model fits relatively well the data, except at longer wavelengths than 100 μm.

Radiative transfer models were also calculated by Henning et al. (1994) with a spherical geometry for the dust envelope. Their model fits well the overall SED, including longer wavelengths than 100 μm. They suggested that the main part of the radiation comes from a spherical dust configuration. More recently, Elia et al. (2004) modelled the continuum emission from the circumstellar environment of some sources using the same code as Henning et al. (1994). Their models were fitted to *ISO* data, considering both, gas and dust arranged in circumstellar spherical shells with temperature and density profiles described by power laws, $T \approx r^{-q}$ and $n \approx r^{-p}$, respectively. They also considered a disc geommetry but they did not fit longer wavelengths.

In our study we have first analysed the photometric data available in the literature and based on the aperture sizes used, we have selected only those points that could be related to star (or the close-by regions) and not contaminated by other sources and/or nebula. Using our code which treats the radiative transfer via the Monte Carlo method for a spherical CSM, we could not reproduce the SED of CD-42°11721. Even using some physical parameters cited by Henning et al. (1994), especially the envelope inner radius, the effective temperature, and density law ($n \approx r^{-1}$), we have obtained unrealistic high grain temperatures (about 7000 K), meaning that the dust could not be located so close to the star. We are aware of the fact that there are several differences between both codes; however, we can point out three of them. First, their model is dependent on the distance of the object (luminosity) and they are assuming a higher value than us for CD-42°11721 ($d = 2$kpc), and secondly they considered two different density distributions inside the envelope, working at different distances from the star. However, the shape of the SED is not only determined by the structure of the circumstellar region, but also by the nature of the grains. Henning et al. (1994) adopted a fluffy dust model to describe dust particles in such a CSM. No small particles were considered, and this is the third difference between our model and Henning's one, and it may be the most important. Usually a fluffy dust model is used to describe the coagulation process in dense cores of molecular clouds (Ossenkopf 1993) and young pre-main-sequence stars, but it is not applicable to hot stars. Therefore, we conclude that a spherically symmetric scenario is ruled out.

Based on our optical analysis and the results described previously, we believe that a non-spherical circumstellar envelope, possibly an equatorial disc, seems to be necessary to explain the SED of CD-42°11721. Considering a flared disc scenario, we cannot model well its SED, especially the near- and the far-IR regions. On the other hand, considering an outflowing disc wind, we could get better results. It is important to cite that a better and even more

conclusive modelling will be obtained only when more data using small apertures, especially from far-IR region, are available.

7 THE NATURE OF CD−42°11721

As we presented in this paper, CD−42°11721 is a very curious object presenting the B[e] phenomenon. Its evolutionary stage is quite doubtful, being considered either a young pre-main-sequence star (HAeB[e]) or an evolved post-main-sequence supergiant (B[e] supergiant) and all this doubt is caused by the complete absence of reliable physical parameters for this star.

In our work, we have first presented an optical analysis of this object, that is based on new low- and high-resolution (highest than previously published) optical spectra of CD−42°11721. Especially the high-resolution spectrum reveals a huge number of emission lines from both, permitted and forbidden transitions. Many of these lines have been detected for the first time. We created a spectral atlas containing the equivalent widths of all measured lines, as well as a profile classification. Line profiles are found to be single-peaked, double-peaked, or (especially lines of Fe II) even multiple-peaked. The presence of atoms mostly neutral or singly ionized and the variety in line profiles speak in favour of a non-spherical density distribution within the CSM close to the central star. The existence of a circumstellar disc is suggested especially by the existence of numerous emission lines from neutral elements.

Using these optical data, we could estimate the stellar parameters of CD−42°11721. We plotted the effective temperature and luminosity obtained by us, into the HR diagram (top panel of Fig. 13) together with known galactic and MC B[e] supergiants, taken from the summary table given in Lamers et al. (1998) and references therein. Also included are evolutionary tracks taken from Schaller et al. (1992) for non-rotating stars with solar metallicity. The position of CD−42°11721 falls into the region of B[e] supergiants ($L_* \geqslant 10^4\,L_\odot$, Lamers et al. 1998) and even coincides with the position of Hen S59, a Large Magellanic Cloud (LMC) B[e] supergiant. While all to-date known galactic B[e] supergiants have $L_* \geqslant 3 \times 10^4\,L_\odot$, there are some low-luminosity objects ($10^4 \leqslant L_*(L_\odot) \leqslant 3 \times 10^4$) in the Magellanic Clouds (Gummersbach, Zickgraf & Wolf 1995), for which CD−42°11721 might be the first galactic low-luminosity counterpart, having evolved from a progenitor star with an initial mass of 8–10 $M_\odot$. With such a mass, the surface gravity becomes $\log g \simeq 3$.

To test a possible pre-main-sequence nature, we plotted the HR diagram for galactic HAeBe stars taken from Berrilli et al. (1992) together with the birthline, the zero-age main-sequence (ZAMS), and pre-main-sequence evolutionary tracks from Bernasconi & Maeder (1996). While the galactic HAeBe stars lie well below the birthline, this is not the case for CD−42°11721, making its classification as an HAeBe star questionable (bottom panel of Fig. 13).

Intending to improve this discussion, we have also made an IR analysis of this star. As shown in Section 4, Acke & van den Ancker (2006) showed that the most detached characteristic of the *ISO* and *IRAS* spectra, the very intense PAH features, actually do not seem to be related to the star itself, but to an envelope or a surrounding nebula. This fact is very important, because the presence of C-rich material implies a C-rich photosphere (Waters et al. 1998) that seems hard to be explained in a supergiant scenario whose spectrum is dominated by several H recombination lines, even knowing that PAH emission was already identified in luminous blue variable (LBV) stars (Voors 1999). In Section 6, we have also presented that our best results for the modelling of CD−42°11721 were obtained considering an outflowing disc wind, typical of B[e] supergiant stars.
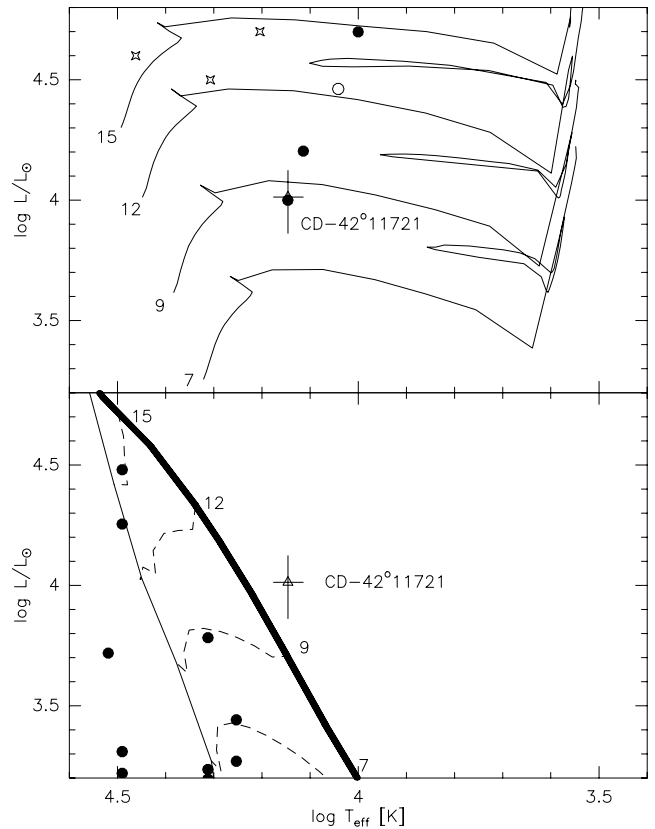
Figure 13. Top panel: the HR diagram for B[e] supergiants in the LMC (filled circles), the Small Magellanic Cloud (open circles), and the Milky Way (asterisks), data from Lamers et al. (1998) and references therein. Also plotted are evolutionary tracks from Schaller et al. (1992) for non-rotating stars with solar metallicity. The location of CD−42°11721 is in agreement of being a post-main-sequence object having evolved from a progenitor star with an initial mass of about 8–10 $M_\odot$. In addition, it lies in the region of well-known B[e] supergiants. Bottom panel: the HR diagram for galactic HAeBe stars (filled circles, Berrilli et al. 1992). The solid line defines the ZAMS, and the thick solid line defines the birthline. CD−42°11721 is plotted as the triangle. It is located above the birthline.

Summarizing, based on our optical and IR analysis (even considering that our errors could be underestimated) and the modelling of the SED, a B[e] supergiant nature seems to us to be a good scenario to explain the observed characteristics of CD−42°11721. However, a young or even pre-main-sequence nature for this curious object could not definitely be excluded by our qualitative analysis.

ACKNOWLEDGMENTS

REFERENCES

Allen C. W., 1973, Astrophysical Quantities, 209
Acke B., van den Ancker M. E., 2004, A&A, 426, 151
Acke B., van den Ancker M. E., 2006, A&A, 457, 171

Acke B., van den Ancker M. E., Dullemond C. P., 2005, A&A, 436, 209

Benedettini M., Nisini B., Giannini T., Lorenzetti D., Tommasi E., Saraceno P., Smith H. A., 1998, A&A, 339, 159

Bernasconi P. A., Maeder A., 1996, A&A, 307, 829

Berrilli F., Corciulo G., Ingrosso G., Lorenzetti D., Nisini B., Strafella F., 1992, ApJ, 398, 254

Borges Fernandes M., 2004, PhD thesis, Observatório Nacional (MCT-Brasil)

Burrows C. J. et al., 1996, ApJ, 473, 437

Carlson E. D., Henize K. G., 1979, Vistas Astron., 23, 213

Chiang E. I., Goldreich P., 1997, ApJ, 490, 368

Cidale L., Zorec J., Tringaniello L., 2001, A&A, 368, 160

David P., Pégourié B., 1995, A&A, 293, 833

de Winter D., Thé P. S., 1990, Ap&SS, 166, 99

de Winter D. et al., 2001, A&A, 380, 609

Dullemond C. P., 2002, A&A, 395, 853

Dullemond C. P., Dominik C., 2004, A&A, 417, 159

Dullemond C. P., Dominik C., Natta A., 2001, ApJ, 560, 957

Egan M. P. et al., 1999, The Midcourse Space Experiment point source catalog version 1.2: Explanatory guide. Air Force Research Laboratory Technical Report, No. AFRL-VS-TR-1999-1522

Elia D., Strafella F., Campeggio L., Giannini T., Lorenzetti D., Nisini B., Pezzuto S., 2004, ApJ, 601, 1000

Elia D., Strafella F., Campeggio L., Maiolo B., Pezzuto S., 2005, New Astron., 10, 545

Fuente. A., Rodríguez-Franco A., Testi L., Natta A., Bachiller R., Neri R., 2004, Ap&SS, 292, 465

Glass I. S., Allen D. A., 1975, Obs, 95, 27

Grady C. A. et al., 2000, ApJ, 544, 895

Gummersbach C. A., Zickgraf F.-J., Wolf B., 1995, A&A, 302, 409

Habart E., Testi L., Natta A., Vanzi L., 2003, A&A, 400, 575

Hamaguchi K., Yamauchi S., Koyama K., 2005, ApJ, 618, 360

Hamann F., Persson S. E., 1989, ApJS, 71, 931

Hamuy M., Suntzeff N. B., Heathcote S. R., Walker A. R., Gigoux P., Phillips M. M., 1994, PASP, 106, 566

Henning Th., Launhardt R., Steinacker J., Thamm E., 1994, A&A, 291, 546

Herbst W., 1975, AJ, 80, 212

Hillenbrand L. A., Strom S. E., Vrba F. J., Keene J., 1992, ApJ, 397, 613

Hutsemékers D., Van Drom E., 1990, A&A, 238, 134

Jaeger C., Molster F. J., Dorschner J., Henning Th., Mutschke H., Waters L. B. F. M., 1998, A&A, 339, 904

Jourdain de Muizon M., d'Hendecourt L. B., Geballe T. R., 1990, A&A, 227, 526

Kenyon S. J., Hartmann L., 1987, ApJ, 322, 293

Kraus M., Borges Fernandes M., de Araújo F. X., Lamers H. J. G. L. M., 2005, A&A, 441, 289

Kurucz R. L., 1979, ApJS, 40, 1

Lamers H. J. G. L. M., Zickgraf F-J., de Winter D., Houziaux L., Zorec J., 1998, A&A, 340, 117

Landaberry S. J. C., Pereira C. B., de Araújo F. X., 2001, A&A, 376, 917

Lopes D. F., Damineli Neto A., de Freitas Pacheco J. A., 1992, A&A, 261, 482

Lorenzetti D. et al., 1999, A&A, 346, 604

Lorenz-Martins S., Pompéia L., 2000, MNRAS, 315, 856

Machado M. A. D., de Araújo F. X., 2003, A&A, 409, 665

Mannings V., 1994, MNRAS, 271, 587

Mannings V., Sargent A. I., 1997, ApJ, 490, 792

Mannings V., Sargent A. I., 2000, ApJ, 529, 391

Mathis J. S., Rumpl W., Nordsieck K. H., 1977, ApJ, 217, 425

McCaughrean M. J., O'Dell C. R., 1996, AJ, 111, 1977

McGregor P. J., Hyland A. R., Hillier D. J., 1988, ApJ, 324, 1071

McKenna F. C., Keenan F. P., Hambly N. C., Allende Prieto C., Rolleston W. R. J., Aller L. H., Feibelman W. A., 1997, ApJS, 109, 225

Meeus G., Waters L. B. F. M., Bouwman J., van den Ancker M. E., Waelkens C., Malfait K., 2001, A&A, 365, 476

Merrill P. W., Burwell C. G., 1949, ApJ, 110, 387

Moore C. E., 1945, A Multiplet Table of Astrophysical Interest, Part I - Table of Multiplets, revised edn. Princeton University Observatory, Princeton, New Jersey

Natta A., Palla F., Butner H. M., Evans N. J. II, Harvey P. M., 1993, ApJ, 406, 674

Ossenkopf V., 1993, A&A, 280, 617

Oudmaijer R. D., Proga D., Drew J. E., de Winter D., 1998, MNRAS, 300, 170

Pagel B. E. J., 1969, Nat, 221, 325

Rouleau F., Martin P. G., 1991, ApJ, 377, 526

Schaller G., Schaerer D., Meynet G., Maeder A., 1992, A&AS, 96, 269

Shore S. N., Brown D. N., Bopp B. W., Robinson C. R., Sanduleak N., Feldman P. D., 1990, ApJS, 73, 461

Skinner S. L., Brown A., Stewart R. T., 1993, ApJS, 87, 217

Swings J. P., 1981, A&A, 98, 112

Thackeray A. D., 1967, MNRAS, 135, 51

Thé P. S., de Winter D., Perez M. R., 1994, A&AS, 104, 315

Voors R. H. M., 1999, PhD thesis, Utrecht University

Waters L. B. F. M., Morris P. W., Voors R. H. M., Lamers H. J. G. L. M., 1998, in Hubert A. M., Jaschek C., eds, Vol. 233. B[e] Stars, Astrophysics and Space Science Library. Kluwer, Boston, p. 111

Winkler H., Wolf B., 1989, A&A, 219, 151

Zhang P., Chen P. S., He J. H., 2004, New Astron., 9, 509

Zickgraf F.-J., 2003, A&A, 408, 257

Zickgraf F.-J., Wolf B., Stahl O., Leitherer C., Klare G., 1985, A&A, 143, 421

APPENDIX A: THE OPTICAL LINE LIST OF CD-42°11721

Table A1. Catalogue of lines identified in the FEROS spectrum of CD-42°11721. Listed are the observed wavelength, equivalent width, description of the line profile (S = single-peaked, D = double-peaked, M = multiple-peaked, A = absorption, Blend = superposition of several lines), and the line identification with the laboratory wavelength.

Wavelength (Å)	W(λ)	Line profile	Identification
3835.3	1.64	S	H9 3835.4
3855.6	1.46	S	Si II (m1) 3856.0
3889.0	3.56	S	He I (m2) 3888.7
			H8 3889.1
3933.5	0.34	A	Ca II (m1) 3933.7
3968.4	0.13	A	Ca II (m1) 3968.5
3969.4	2.33	S	Hϵ 3970.1
4068.3	0.22	S	[S II] (m1F) 4068.6
4101.7	4.61	S	Hδ 4101.7
4173.3	0.51	S	Fe II (m27) 4173.5
4178.5	0.75	S	Fe II (m21) 4177.7
4233.0	1.70	S	Fe II (m27) 4233.2
4243.4	0.50	S	[Fe II] (m21F) 4244.0
4258.0	0.22	S	Fe II (m28) 4258.2
4276.4	0.14	S	[Fe II] (m21F) 4276.8
4287.0	0.57	S	[Fe II] (m7F) 4287.4
4290.1	0.13	S	Ti II (m41) 4290.2
			Ne II (m57) 4290.4
4296.3	0.36	D	Fe II (m28) 4296.6
4303.0	0.48	S	Fe II (m27) 4303.2
4340.5	8.76	S	Hγ 4340.5
4351.5	1.24	S	Fe II (m27) 4351.8
4358.8	0.46	S	[Fe II] (m7F) 4359.3
4384.7	1.31	D	Mg II 4384.6
4413.5	0.62	S	[Fe II] (m7F) 4413.8
4416.4	2.15	S	[Fe II] (m6F) 4414.5
			[Fe II] (m6F) 4416.3

Table A1 – *continued*

Wavelength (Å)	W(λ)	Line profile	Identification
			Fe II (m27) 4416.8
4451.7	0.30	S	[Fe II] (m32F) 4452.1
4457.7	0.18	S	[Fe II] (m6F) 4458.0
4472.4	0.71	S	He I (m14) 4471.7
4481.1	0.98	S	Mg II (m4) 4481.3
4489.0	0.50	D	[Fe II] (m6F) 4488.8
4491.2	0.63	D	Fe II (m37) 4491.4
4508.1	0.80	Blend	Fe II (m38) 4508.3
			Fe II [m6F] 4509.6
4515.1	1.01	M	[Fe II] (m6F) 4514.9
4520.0	1.05	D	Fe II (m37) 4520.2
4522.4	1.08	D	Fe II (m38) 4522.6
4533.9	0.25	S	Fe II (m37) 4534.2
4541.3	0.36	S	Fe II (m38) 4541.5
4549.3	2.07	D	Fe II (m38) 4549.5
4555.6	1.14	M	Fe II (m37) 4555.9
4558.3	0.36	D	Fe II (m20) 4558.6
4576.1	0.29	D	Uid
4583.5	2.71	Blend	Fe II (m37) 4582.8
			Fe II (m38) 4583.8
			Fe II (m26) 4584.0
4588.0	0.18	S	Cr II (m44) 4588.2
			Cr II (m16) 4588.4
4618.5	0.17	S	C II 4618.9
4620.3	0.32	S	Fe II (m38) 4620.5
			N II (m5) 4621.4
4629.1	2.03	D	Fe II (m37) 4629.3
4634.5	0.37	S	Fe II (m25) 4634.6
4639.4	0.11	S	O II (m1) 4638.9
4657.0	0.24	S	Fe II (m43) 4657.0
4666.5	0.39	D	Fe II (m26) 4665.8
4727.7	0.19	S	[Fe II] (m4F) 4728.1
4731.2	0.40	D	Fe II (m43) 4731.4
4814.2	0.28	S	[Fe II] (m20F) 4814.6
4823.9	0.25	D	Cr II (m30) 4824.1
			S II (m52) 4824.1
4847.9	0.22	S	Fe II (m30) 4847.6
4861.4	30.41	D	Hβ 4861.3
4889.3	0.24	S	[Fe II] (m4F) 4889.6
			[Fe II] (m3F) 4889.7
4905.0	0.16	S	[Fe II] (m20F) 4905.4
4923.7	3.63	M	Fe II (m42) 4923.9
5018.1	4.76	D	Fe II (m42) 5018.4
5041.5	0.49	S	Si II (m5) 5041.1
5056.1	0.64	S	Si II (m5) 5056.4
5100.5	0.15	S	Fe II 5101.0
5111.1	0.15	S	[Fe II] (m19F) 5111.6
5145.6	0.25	S	C II (m16) 5145.2
			Fe II (m35) 5146.1
5149.1	0.08	S	Fe II 5149.5
5158.3	0.55	M	[Fe II] (m18F) 5158.0
5163.6	0.09	S	[Fe II] (m35F) 5163.9
5168.9	3.87	D	Fe II (m42) 5169.0
5183.4	0.09	S	Mg I (m2) 5183.6
5197.4	1.98	D	Fe II (m49) 5197.6
5203.4	0.10	S	Uid
5227.1	0.16	S	Fe III 5227.5
5234.5	2.41	D	Fe II (m49) 5234.6
5237.0	1.01	S	Uid
5248.5	0.25	S	Fe II 5248.0
5254.6	0.30	D	Fe II (m49) 5254.9
5256.8	0.09	S	[Cr II] (m13F) 5256.0
5261.5	0.38	D	[Fe II] (m19F) 5261.6

Wavelength (Å)	W(λ)	Line profile	Identification
5264.5	0.38	S	Mg II 5264.3
			Fe II (m48) 5264.8
5268.5	0.11	S	[Fe III] (m1F) 5270.4
5273.0	0.21	S	C III 5272.6
5273.1	0.41	S	[Fe II] (m18F) 5273.4
5275.7	1.85	D	Fe II (m49) 5276.0
5283.8	0.57	D	[Fe II] (m35F) 5283.1
5291.6	0.10	S	Fe III 5291.8
5296.5	0.06	S	[Fe II] (m19F) 5296.8
5298.7	0.08	S	Uid
5316.3	3.99	D	Fe II (m49) 5316.6
5325.3	0.24	D	Fe II (m49) 5325.6
5333.4	0.20	S	[Fe II] (m19F) 5333.7
5346.6	0.21	S	Fe II (m49) 5346.6
			[Fe II] (m18F) 5347.7
5362.6	1.20	Blend	[Fe II] (m17F) 5362.1
			Fe II (m48) 5362.9
5376.0	0.16	S	[Fe II] (m19F) 5376.5
5402.0	0.13	S	Mg II (m24) 5401.1
5413.2	0.21	S	[Fe III] (m1F) 5412.0
5425.0	0.35	D	Fe II (m49) 5425.3
5432.7	0.22	S	Fe II (m55) 5432.9
			[Fe II] [(m18F) 5433.2
5466.6	0.25	S	Fe II 5466.0
5502.8	0.13	S	Uid
5510.7	0.11	S	Cr II (m23) 5510.7
5527.0	0.19	S	[Fe II] (m17F) 5527.3
			[Fe II] (m34F) 5527.6
5529.5	0.22	S	Uid
5534.5	1.00	D	Fe II (m55) 5534.9
5543.8	0.08	S	Uid
5576.7	0.84	S	[O I] (m3) 5577.3
5746.5	0.10	S	[Fe II] (m34F) 5747.0
5754.2	0.07	S	[N II] (m3F) 5754.8
5780.4	0.44	A	DIB
5791.7	0.08	S	C I (m18) 5793.5
5797.0	0.16	A	DIB
5835.1	0.07	S	Fe II (m58) 5835.4
5849.7	0.05	A	DIB
5876.0	2.00	S	He I (m11) 5875.6
5889.7	0.65	A	Na I (m1) 5890.0
5895.7	0.58	A	Na I (m1) 5895.9
5957.3	0.50	S	Si II (m4) 5957.6
5978.9	0.85	S	Fe III (m117) 5978.9
			Si II (m4) 5979.0
5991.0	0.27	M	Fe II (m46) 5991.4
6040.3	0.13	S	Uid
6045.9	0.21	S	S I (m10) 6046.0
			O II 6046.3
			O II 6046.5
6083.7	0.13	S	Fe II (m46) 6084.1
6103.2	0.06	S	Fe II (m200) 6103.5
6125.2	0.30	S	Mn II (m13) 6125.9
6130.1	0.32	S	Mn II (m13) 6129.0
			Fe II (m46) 6129.7
6148.2	0.72	M	Fe II (m74) 6147.7
6158.0	0.50	S	O I (m10) 6156.0
			O I (m10) 6156.8
			O I (m10) 6158.2
6160.8	0.14	S	Fe II (m161) 6160.8
6172.7	0.15	S	N II (m36) 6173.4
6195.8	0.06	A	DIB
6202.9	0.09	A	DIB

Table A1 – *continued*

Wavelength (Å)	W(λ)	Line profile	Identification
6233.2	0.25	M	Fe II 6233.5
6238.3	0.49	D	Fe II (m74) 6238.4
6247.8	1.40	M	Fe II (m74) 6247.6
6291.5	0.15	S	Uid
6299.8	1.20	D	[O I] (m1F) 6300.3
6317.8	2.17	D	Fe 6318.0
6338.0	0.13	S	Uid
6347.0	1.73	S	Si II (m2) 6347.1
6356.8	0.16	S	Uid
6363.3	0.43	D	[O I] (m1F) 6363.8
6371.1	1.39	S	Fe II (m40) 6369.5
			Si II (m2) 6371.4
6384.1	2.30	M	Fe II 6383.8
6416.6	0.47	D	Fe II (m74) 6416.9
6432.3	0.29	D	Fe II (m40) 6432.7
6442.7	0.49	D	Fe II 6443.0
6456.0	1.94	Blend	O I (m9) 6456.0
			Fe II (m74) 6456.4
6465.5	0.06	S	Uid
6483.4	0.41	S	N I (m21) 6482.7
			N I (m21) 6483.8
			N I (m21) 6484.9
6492.2	1.04	Blend	Fe 6491.3
			Fe 6493.1
6506.1	0.35	D	Fe II 6506.3
6516.2	1.25	M	Fe II (m40) 6516.1
6547.5	0.05	S	[N II] (m1F) 6548.1
6562.9	194.30	D	Hα 6562.8
6582.9	0.15	S	[N II] (m1F) 6583.6
6586.4	0.38	D	C I (m22) 6587.8
6598.5	0.22	S	Uid
6613.5	0.15	A	Uid
6626.5	0.12	S	Uid
6658.3	0.09	S	Uid
6666.2	0.21	S	[Ni II] (m2F) 6666.8
6678.7	1.08	S	He I (m46) 6678.2
6716.0	0.08	S	[S II] (m2F) 6716.4
6730.3	0.10	S	[S II] (m2F) 6730.8
6776.3	0.08	S	Fe II (m210) 6777.3
6814.3	0.12	S	C II 6812.2
7001.8	0.22	S	O I (m21) 7001.9
			O I (m21) 7002.2
7041.9	0.14	S	Uid
7065.6	1.02	S	He I (m10) 7065.2
7109.1	0.10	S	Uid
7154.6	0.47	D	[Fe II] (m14F) 7155.1
7171.5	0.10	S	[Fe II] (m14F) 7171.9
7308.1	0.15	S	Fe II (m73) 7308.0
7320.1	0.16	S	[O II] (m2F) 7318.6
7329.6	0.09	S	[O II] (m2F) 7329.9
7377.3	0.30	S	[Ni II] (m2F) 7377.9
7387.2	0.33	M	[Fe II] (m14F) 7388.2
7409.3	0.34	M	Fe II 7409.0
7423.2	0.13	S	N I (m3) 7423.6
7442.0	0.20	S	N I (m3) 7442.3
7449.0	0.14	D	Fe II (m73) 7449.3
7452.0	0.19	S	[Fe II] (m14F) 7452.5
7461.9	0.57	M	Fe II (m73) 7462.4
7467.7	0.25	D	N I (m3) 7468.3
7479.5	0.07	S	Fe II (m72) 7479.7
7495.4	0.62	D	Uid
7499.8	0.40	D	Uid
7506.4	0.21	D	Uid

Table A1 – *continued*

Wavelength (Å)	W(λ)	Line profile	Identification
7514.1	1.99	M	Fe II (m73) 7515.9
7520.3	0.07	S	Fe II 7520.7
7533.0	0.10	D	Fe II (m72) 7533.4
7561.9	0.08	A	Uid
7572.1	0.33	M	Fe II 7571.7
7578.8	0.20	D	Uid
7587.4	0.07	S	Uid
7711.2	2.32	D	Fe II (m73) 7711.7
7731.6	0.43	S	Fe II 7731.7
7755.2	0.20	D	Fe II 7755.6
7764.1	0.07	S	[Fe II] (m30F) 7764.7
7773.5	6.08	Blend	O I (m1) 7772.0
			O I (m1) 7774.2
			O I (m1) 7775.4
7780.0	0.13	S	Fe II 7780.4
7788.9	0.10	D	Fe 7789.3
7800.9	0.25	D	Fe 7801.2
7818.2	0.16	D	Fe 7817.9
7835.6	0.18	M	Fe 7835.9
7851.4	0.27	S	Fe 7851.9
7866.2	1.46	D	Fe 7866.5
7877.0	1.02	D	Mg II 7877.1
7896.3	1.57	D	Mg II (m8) 7896.4
7917.4	0.60	D	Fe II 7917.8
7970.1	0.08	S	Fe II 7970.4
7975.5	0.60	D	Fe II 7975.9
7981.8	0.11	S	O I 7982.0
			O I 7982.4
8030.0	0.18	S	Fe II 8030.5
8083.4	0.29	D	Fe II 8083.9
8090.4	0.06	D	S II (m69) 8089.9
			[Ti I] (m18F) 8091.8
8092.7	0.14	D	Fe II 8092.2
8096.4	0.35	M	Uid
8101.2	0.19	D	Fe II 8101.5
8106.4	0.42	M	[Cr II] (m20F) 8106.9
8109.9	0.48	D	[Cr II] 8110.4
8113.1	0.05	S	Uid
8114.9	0.11	S	Uid
8215.1	0.62	S	N I (m2) 8216.8
8234.7	0.60	S	Mg II (m7) 8234.6
8242.8	0.02	S	N I (m2) 8242.3
8249.9	0.38	S	P40 8250.0
8267.7	0.17	S	P34 8267.9
8292.0	0.31	S	P29 8292.3
8298.6	0.83	S	P28 8298.8
8323.5	1.13	S	P25 8323.4
8333.6	1.49	S	P24 8334.0
8345.2	2.05	S	P23 8346.0
8358.5	2.70	S	P22 8359.0
8374.3	2.80	S	P21 8374.5
8392.2	3.34	S	P20 8392.4
8413.1	3.62	S	P19 8413.3
8437.7	4.58	S	P18 8438.0
8445.9	35.62	S	O I (m4) 8446.8
8467.4	6.31	S	P17 8467.3
8489.8	1.72	S	Fe II 8490.1
8501.7	9.96	S	P16 8502.5
8567.2	0.19	S	N I (m8) 8567.7
8598.2	10.77	S	P14 8598.4
8608.9	0.14	S	Fe 8609.5
8616.3	0.26	S	[Fe II] (m13F) 8617.0
8628.9	1.08	D	N I (m8) 8629.2

Table A1 – *continued*

Wavelength (Å)	W(λ)	Line profile	Identification
8636.1	0.37	S	Fe II 8636.6
8648.5	0.32	S	Uid
8655.4	0.19	S	N I (m8) 8655.9
8664.4	12.00	S	P13 8665.0
8680.0	1.18	D	N I (m1) 8680.2
			S I (m6) 8680.5
8682.9	0.88	S	N I (m1) 8683.4
8685.4	0.62	S	N I (m1) 8686.1
8694.6	0.27	S	S I (m6) 8694.7
			Fe II 8695.1
8702.9	0.46	S	N I (m1) 8703.2
8711.2	0.45	S	N I (m1) 8711.7
8718.6	0.52	S	N I (m1) 8718.8
8721.9	0.42	S	Fe II 8722.4
8728.1	0.25	S	[C I] (m3F) 8727.4
			N I (m1) 8728.9
8750.2	11.50	S	P12 8750.5
8767.8	0.57	S	Uid
8774.4	0.09	S	Uid
8783.8	0.32	S	Uid
8805.6	0.57	S	Fe II 8805.1
8813.6	0.38	S	Fe II 8813.4
8819.3	0.35	S	Uid
8827.4	0.98	S	Fe II 8825.5
			Fe II 8829.8

Table A1 – *continued*

Wavelength (Å)	W(λ)	Line profile	Identification
8833.5	0.26	S	Fe II 8834.0
8906.1	0.17	S	Uid
8911.4	0.62	S	Fe II 8912.5
8915.9	0.29	S	Fe II 8916.3
8926.2	2.93	D	Fe II 8926.7
9014.6	11.80	S	P10 9014.9
9060.4	0.72	S	Fe II 9060.0
			N I (m15) 9060.6
			C I (m3) 9061.5
			C I (m3) 9062.5
9070.7	0.20	S	[S III] (m1F) 9069.4
9075.8	2.11	S	Fe II 9075.5
9094.5	1.43	S	C I (m3) 9094.9
9111.5	0.68	S	C I (m3) 9111.9
9122.7	2.47	D	Fe II 9122.9
9132.2	1.40	S	Fe II 9132.4
9177.1	3.20	D	Fe II 9178.0
9187.1	0.98	S	Fe II 9187.2
9196.9	0.76	S	Fe II 9196.9
9203.3	2.89	S	Fe II 9203.1

This paper has been typeset from a TEX/LATEX file prepared by the author.